



## Molten salt induced corrosion of Inconel 625 superalloy in $\text{PbSO}_4\text{-Pb}_3\text{O}_4\text{-PbCl}_2\text{-Fe}_2\text{O}_3\text{-ZnO}$ environment

E. Mohammadi Zahraei\*, A.M. Alfantazi

Corrosion Research Group, Department of Materials Engineering, The University of British Columbia, 309-6350 Stores Road, Vancouver, B.C., Canada V6T 1Z4

### ARTICLE INFO

#### Article history:

Received 9 March 2012

Accepted 14 August 2012

Available online 24 August 2012

#### Keywords:

A. Molten salt

A. Superalloys

B. EIS

B. XRD

C. High temperature corrosion

C. Oxidation

### ABSTRACT

Corrosion behavior of alloy 625 was studied in a molten salt consisting of  $47\text{PbSO}_4\text{-}23\text{ ZnO}\text{-}13\text{ Pb}_3\text{O}_4\text{-}10\text{Fe}_2\text{O}_3\text{-}7\text{PbCl}_2$  (wt.%) under air atmosphere at 600, 700 and 800 °C, utilizing OCP, potentiodynamic polarization, EIS and weight-loss measurement techniques. Phase structure, morphology and chemical analysis of corrosion products and scales were characterized by means of XRD, SEM/EDX, and ICP/AAS.

General surface corrosion, intergranular corrosion, formation of voids and, a network of distributed pores on surface and cross-section, plus internal oxidation and sulfidation were identified as different modes of corrosion attack. EIS data fit to a porous and non-protective barrier layer electrochemical model.

© 2012 Elsevier Ltd. All rights reserved.

### 1. Introduction

Superalloys are high temperature materials which display resistance to mechanical (fatigue and creep) and chemical degradation at temperatures close to their melting point. They are often based upon nickel, but contain significant amounts of at least ten other elements including chromium, molybdenum, and niobium [1,2]. Nickel-based alloys have emerged for high temperature applications because nickel has a face-centered cubic (FCC) crystal structure and it is thus both ductile and tough. FCC metals have high symmetry. Moreover, they contain four distinct (nonparallel) close-packed slip planes of the form {111} and three close-packed slip directions of the form ⟨110⟩ within each plane, giving a total of 12 slip systems. Accordingly, there is a wide choice of slip systems when a FCC metal undergoes deformation and at least one slip system is favorably orientated for slip to occur at low applied stresses, causing FCC metals to have high ductility and toughness [3–5]. Furthermore, nickel is stable in the FCC crystallographic structure from ambient temperature up to its melting point; as a result, no contraction/expansion can occur due to a phase transformation [6]. Alloy 625 is a high-chromium, high-molybdenum, nickel-based superalloy, which has been widely used in form of bulk [7,8], weld-overlay [9,10], and plasma-sprayed [11,12] coatings for high temperature applications in many corrosive environments: gas turbines, waste-fired boilers as well as pulp and paper industries, to name but a few. Preventing high temperature

oxidation and hot corrosion at elevated temperatures due to oxidation resistance of alloy 625 is the main purpose for such a broad range of applications [13].

High nickel content has given satisfactory results in mechanical performance of alloy 625 but when chromium oxide layer is dissolved by a corrosive environment, nickel oxide is developed together with other metallic oxides [14,15]. High chromium content provides good resistance to oxidation and molten salt-induced corrosion at high temperatures mainly due to formation of a protective chromium-rich oxide layer. Chromium is one of the most effective alloying elements to act against corrosion, necessitating at least 18 to 24 wt.% to optimize its effectiveness [16–18]. Significant content of molybdenum makes alloy 625 resistant to pitting and crevice corrosion; whereas a combined nickel and molybdenum content makes it resistant to non-oxidizing environments and crevice corrosion [19]. Alloying with niobium has stabilized it against sensitization during welding, thereby preventing subsequent intergranular attack [20,21]. Also, niobium and tantalum stabilization makes this alloy suitable for corrosion service in as-welded conditions. Furthermore, alloy 625 has an appropriate resistance to chloride corrosion cracking [16]. High concentrations of chromium and molybdenum, as well as presence of niobium, which cause formation of a  $\text{Cr}_2\text{O}_3$  protective film together with  $\text{NiO}$ ,  $\text{Nb}_2\text{O}_5$  and  $\text{NbCrO}_4$  and in some cases a Cr-Mo- and Nb-rich layer, are the most important compositional and microstructural features of alloy 625 [22]. Despite the fact that superalloys, particularly alloy 625, have been developed for high-temperature applications, these alloys are not always able to meet simultaneous high-temperature strength and high-temperature corrosion resistance requirements in certain applications [15].

\* Corresponding author. Tel.: +1 604 822 8745; fax: +1 604 822 3619.

E-mail address: ehsanmoh@interchange.ubc.ca (E. Mohammadi Zahraei).

Alloys used in some environments, such as power generation machines, gas turbines, waste-to-energy boilers (WTE), industrial waste incinerators, pulp and paper industries, coal-fired boilers, oil-fired boilers, KIVCET flash smelter boilers, furnaces, and black liquor recovery boilers, sometimes undergo an aggressive mode of corrosion attack associated with formation of salt deposits on their surfaces at elevated temperatures. This deposit-induced accelerated oxidation is called “hot corrosion” [23]. Reportedly, 5–10% of operating costs in such plants are attributed to high temperature corrosion failure and related maintenance costs [24,25].

Hot corrosion is the most prevalent mode of attack at high temperature, in particular where surface of alloy is covered by a layer of a deposited salt mixture. At elevated temperatures, the deposited salt mixture can be a liquid phase at the beginning of deposition, known as molten salt-induced corrosion or type I hot corrosion; or it can be a solid phase at the onset of deposition, and then be altered to form a liquid phase after being exposed to an alloy because of reaction with environment, this is known as type (II) hot corrosion [26,27]. Numerous variables, including composition and amount of deposit, gas composition, temperature, temperature cycling, erosion, alloy composition, and alloy microstructure, have direct effects on severity of hot corrosion [28]. Severity of corrosive environments at metal/molten salt interface is influenced by penetration depth of corrosive species through scales. Protective oxide films, derived from alloying elements, play an important role in preventing corrosion attack [29]. As a result of this corrosion phenomenon, a porous and poorly adherent oxide scale is formed on surface of attacked alloy, which does not have an acceptable capability to protect the alloy in harsh, corrosive conditions [30]. During type (I) hot corrosion, after chromium-depletion at surface of alloy during initiation stage, oxidation and sulfidation of base material accelerate and a porous, non-protective oxide layer forms in final stage of attack (propagation) [31,32]. Effect of temperature fluctuation as well as gas temperature on corrosion behavior of an alloy 625 weld overlay on surface of SA 213 in WTE plants was evaluated by Kawahara [33]. Corrosion was accelerated by breakdown of protective oxide layer due to thermal stresses that resulted from differences in thermal expansion of substrate and its weld metal [33].

Despite wide range of alloy 625 usage at high temperature to protect water-wall tubes of different types of boilers against molten salt-induced corrosion and to reduce corrosion rate of boiler tubes in other energy-production applications [15,34,35], there is still no systematic study on corrosion performance of alloy 625 at high temperatures when heavy metals such as lead, zinc, and iron, together with chlorine, oxygen, and sulfur are present in molten salt medium. Because of strict economic considerations in these kinds of plants, costs related to maintenance of plant (including hot corrosion failure costs), and related downtime and periodic shutdowns must be reduced as much as possible. Thus, developing a better understanding of high temperature corrosion behavior of alloy 625 in a corrosive molten salt environment containing lead, zinc, iron, as well as sulfur, oxygen, and chlorine, is of important economic value, and scientific interest.

## 2. Experimental procedure

### 2.1. Preparation of working electrode

Alloy 625 working electrodes had a rectangular shape with dimensions of  $20 \times 10 \times 2$  mm. Chemical composition of the alloy was determined by inductively coupled plasma/atomic absorption spectroscopy (ICP/AAS: Inspectorate-International Plasma Laboratory, IPL, BC, Canada). To observe the microstructure of the wrought alloy 625 in as-received condition, one sample was

polished, and then etched in a solution containing 5 ml  $\text{H}_2\text{SO}_4$ , 3 ml  $\text{HNO}_3$  and 92 ml HCl for 35 s [36]. The etched sample was examined by optical microscopy and SEM/EDX. Preparation of specimens for metallographic study was done based on ASTM E3-11 [37]. Mean grain size of the wrought alloy 625 was measured by lineal intersection method [38]. For preparation of the working electrodes, the rectangular pieces of the alloy 625 were ground to 1200-grit silicon carbide paper, rinsed with distilled water, ultrasonically degreased with acetone and dried under a warm air stream. A wire made of 80Cr-20Ni (wt.%) was spot welded to each sample to provide an electrical connection between the working electrode and potentiostat. Alumina tubes were used to isolate the 80Cr-20Ni wire and gap between the alumina tube and the wire was filled with refractory cement (Ceramabond: Are-mco Products, Inc., NY, USA). Use of specimens ground to 1200 and/or 4000-grit [39–42] silicon carbide paper and even polishing with a diamond paste (6 and/or 1  $\mu\text{m}$ ) [43,44] were reported in corrosion studies, in particular molten salt-induced corrosion and high temperature oxidation. In fact, there are no specific instructions for grounding and preparation of specimens for molten salt-induced corrosion study.

### 2.2. Molten salt electrolyte medium

Analytical-grade  $\text{PbSO}_4$  and  $\text{Fe}_2\text{O}_3$  (Sigma-Aldrich, MO, USA),  $\text{Pb}_3\text{O}_4$  (Alfa Aesar, MA, USA),  $\text{PbCl}_2$  (Anachemia, QC, Canada) and  $\text{ZnO}$  (Fisher Scientific, NH, USA) were used to prepare the simulated salt mixture. For preparation of the simulated salt mixture, the measured amounts of the necessary chemical compounds (Table 1) were milled to ensure homogeneity. Elemental analysis of the simulated salt mixture is presented in Table 2. The as-prepared simulated salt mixture was examined by differential thermal analysis (DTA: Linseis L70/2171, Linseis Inc., Selb, Germany) in an air atmosphere from ambient temperature to 1100 °C at a heating rate of  $10^\circ\text{C min}^{-1}$  to evaluate thermal behavior of the mixture and to determine its liquidus temperature. The reason for choosing this specific salt mixture was discussed in our previous reports [15,34]. In summary, the composition of the simulated salt mixture was selected based on chemical composition of corrosive salt mixtures deposited on water-wall tubes of radiant boilers in KIVCET lead and zinc smelters. Details of chemical and phase characterization of these deposited corrosive salts were extensively discussed elsewhere [15]. The heavy metals including Pb, Zn, and Fe, together with S and Cl are the dominant elements, playing a leading role in formation of low melting point phases in the radiant boilers of the KIVCET smelters. The KIVCET lead and zinc smelters are used in service as a modern direct smelting process [45,46].

### 2.3. Platinum pseudo-reference electrode

Electrochemical cell was constituted by the working electrode (alloy 625), and two 1.2 mm diameter/500 mm long platinum wires as auxiliary and pseudo-reference electrodes which immersed directly in the molten salt medium. The platinum wires were woven together to produce a mesh-like counter electrode. Redox electrochemical couple of the platinum pseudo-reference electrode was not identified in the current study. The mesh-like

**Table 1**  
Chemical composition (wt.%) of the prepared simulated salt mixture.

	$\text{PbSO}_4$	$\text{PbCl}_2$	$\text{Pb}_3\text{O}_4$	$\text{ZnO}$	$\text{Fe}_2\text{O}_3$
Salt Mixture	47	7	13	23	10

**Table 2**

Elemental analysis (wt.%) of the prepared simulated salt mixture.

	Pb	Cl	S	Zn	Fe
Salt Mixture	48.1	1.7	5	18.6	3.5

counter electrode (CE) to the working electrode (WE) surface ratio was equal to 5 (CE:WE = 5:1). The platinum electrodes were cleaned, abraded using 600-grit silicon carbide paper, ultrasonically washed in ethanol and then in acetone, and dried under a warm air stream before being isolated in the alumina tubes and sealed with the refractory cement, leaving 25 mm-long free length to make direct contact with the molten salt medium. The alumina tubes, which used for preparation of the pseudo-reference, the counter and the working electrodes, were replaced after each test. All the potentials cited in the text are given versus pure platinum as the pseudo-reference electrode. It should be noted that selection of a correct reference electrode has been always a major issue in molten salt-induced corrosion study [47]. Particularly in the current study finding a suitable candidate that can successfully serve as reference and counter electrode was very challenging due to the extreme harshness, toxicity, and novelty of the molten salt medium. Because of the novelty of the corrosive medium, there were no prior experiences or knowledge about a suitable reference and counter electrode that can demonstrate acceptable performance, stability and durability. For this reason, in the current study, a number of reference electrode systems were tested such as pure silver, pure platinum, platinum – 30 wt.% iridium and platinum – 10 wt.% ruthenium. However, pure platinum demonstrated the best response, stability and durability. The stability of the pure platinum wire as pseudo-reference electrode in the molten salt mixture was confirmed by ICP/AAS, SEM/EDX and XRD techniques as well as weight-loss measurement method. Results will be discussed in Section 3.8. Reportedly, the platinum pseudo-reference electrode satisfies three conditions including fast kinetic, well-known redox couple and constant potential [47]. Also, application of pure platinum as counter and reference electrode has been widely reported in literature, which will be discussed in Section 3.8.

Silver wire dipped into a molten salt-containing silver cations ( $\text{Ag}^+$ ) such as silver chloride ( $\text{AgCl}$ ), was another candidate to be used as reference electrode [47,48].  $\text{Ag}^+$ -containing salt must be separated from molten salt medium by a conductive membrane to have ionic continuity with it [47]. The two potential membrane materials, which were considered to create this electrode, were yttria-stabilized zirconia and alumina. However, none of them can demonstrate an acceptable performance, stability, and appropriate durability in the 47  $\text{PbSO}_4$ –23  $\text{ZnO}$ –13  $\text{Pb}_3\text{O}_4$ –10  $\text{Fe}_2\text{O}_3$ –7  $\text{PbCl}_2$  (wt.%) molten salt medium. Because of the inhomogeneous nature of the molten salt medium, pores of the porous membrane would be blocked at high temperature and the membrane cannot successfully play its role in such an inhomogeneous system. The molten salt system was inhomogeneous because it did not have a specific melting point and it was melted in a wide temperature range. Also, the conductive membranes must be manufactured in laboratory because they are not commercially available [47]. Because of these technical limitations, this type of reference electrode was not examined.

#### 2.4. Electrochemical techniques and weight-loss measurement

The specific amounts of the simulated salt mixture ( $15 \text{ g cm}^{-2}$  of the initial area of the specimen) were introduced into a 30 ml alumina crucible, to give a melt depth of about 3.5 cm. The crucible

was then set inside a vertical electrical furnace to reach the test temperature, which was measured constantly during the tests using a type K thermocouple under a dynamic air atmosphere (flow rate:  $200 \text{ ml min}^{-1}$ ). The crucible and the solid corrosive salt mixture were replaced for each experiment. The potentiostat used in the electrochemical experiments was a Princeton Applied Research (PAR) model 273A with M352 analysis software. Open-circuit potential (OCP), potentiodynamic polarization test as well as electrochemical impedance spectroscopy (EIS) were conducted in the molten salt medium at 600, 700 and 800 °C, in the three-electrode electrochemical cell arrangement. Once the crucible containing the simulated salt mixture was set into the electrical tube furnace, the electrochemical cell was introduced inside the crucible, and the corresponding wires of the potentiostat were connected to the electrochemical cell. The OCP was recorded during the first 24 h of immersion. Before performing the potentiodynamic polarization and the EIS tests, the OCP of the cell must reach a stable value and the system should be at an equilibrium condition. Afterward, impedance measurements were carried out in a frequency range from 50 kHz to 1 mHz with the AC voltage amplitude of  $\pm 5 \text{ mV}$  with respect to the OCP. In the potentiodynamic polarization test, the potential of the working electrode was continuously increased from  $-200$  to  $+1200 \text{ mV}$  with respect to the OCP at the scan rate of  $0.166 \text{ mV/s}$ . Selection of the potential sweep rate of  $0.6 \text{ V/h}$  ( $0.166 \text{ mV/s}$ ) for performing the polarization test was based on the requirements of ASTM G59–97 [49] and ASTM G5–94 [50]. It should be noted that a different fresh working electrode was used for each electrochemical test. Electrochemical determination of the corrosion current density ( $i_{\text{corr}}$ ) as well as the anodic and the cathodic Tafel slopes ( $\beta_a$  and  $\beta_c$ ) by the Tafel extrapolation technique was not possible because the obtained potentiodynamic polarization curves, in log representation, did not show a decade of linearity (Tafel region) even in the cathodic branch. Weight-loss measurement has been widely used as the most accurate and precise method for corrosion rate determination [51]. In this method, relatively simple procedure and easy experimentation reduce the probability of introducing systematic errors into the obtained results [51]. In order to examine the corrosion rate of the alloy 625 through the standard weight-loss measurement (gravimetric) method, embedded test was carried out under the same experimental condition than that for the electrochemical tests, considering the standard procedure presented in ASTM G1–03 [52] and ASTM G31–72 [53]. The schematic of the embedded test was reported by Kawahara [29]. Once the initial weights and dimensions of the specimens were measured and the samples were ultrasonically washed in acetone, the samples were exposed to the molten salt mixture in a 30 ml alumina crucible. At each temperature, three specimens were tested in different crucibles, under the identical conditions, to control the precision of the final weight-loss measurement data. After 24 h exposure to the molten salt medium at 600, 700 and 800 °C, the corroded samples were taken out of the furnace and cooled down in static air. In order to measure the weight-loss of the corroded samples after the embedded test, it is essential to completely remove the scales and the corrosion products from the corroded surfaces. Accordingly, the corroded samples were scraped using a wire brush, mechanically cleaned under a compressed air stream, washed in boiling distilled water and ultrasonically cleaned in alcohol for removing loose and bulky corrosion products and deposits. The corrosion products and the scales strongly adhered to the corroded samples. Consequently, it was not possible to perfectly remove all the corrosion products and the scales from the surface of the corroded sample through a physical technique. Therefore, the rest of the scales were chemically removed according to the standard methodology presented in ASTM G1–03 [52]. After being perfectly cleaned and dried, the corroded specimens were weighed by an electronic

balance with sensitivity of  $10^{-4}$  g. The corrosion mass loss ( $\Delta W$ ) was determined by subtracting the mass of the corroded specimen after removal of the scales and corrosion products from the initial mass of the specimen. The corrosion rate was reported as millimeter per year (mm/year), calculated by using the following equation [52]:

$$\text{Corrosion Rate(mm/year)} = K \left( \frac{\Delta W}{DAT} \right) \quad (1)$$

where:  $K = 87600$  (a constant),  $T$  = time of exposure (hr),  $A$  = surface area ( $\text{cm}^2$ ),  $\Delta W$  = mass loss (g),  $D$  = density =  $8.44 \text{ g cm}^{-3}$  (for alloy 625).

### 2.5. Characterization techniques

At the end of the EIS test, the working electrode had been taken out of the furnace before it was characterized by the scanning electron microscopy with light metal energy-dispersive X-ray spectroscopy (SEM/EDX: Hitachi S-3000N, Tokyo, Japan). The SEM was used to study the surfaces and cross-section of the corroded samples after the EIS test in which it can be considered just a slight potential perturbation, which means almost free corrosion condition. In order to study the morphology and the chemical composition of the scales and the corrosion products, the corroded sample immediately placed in SEM chamber to be analyzed, after the EIS test. It should be noted that for determining the type and the mechanism of the corrosion attack, the scales and the corrosion products must be removed from the corroded surfaces. For this purpose, the corroded sample was physically cleaned under the compressed air stream and washed in boiling distilled water for 30 min, followed by the ultrasonic cleaning in a bath of alcohol for 1 h to remove the loose and bulky corrosion products and the deposits. Then, the standard methodology presented in ASTM G1-03 [52] was followed to chemically remove the rest of the scales. This standard methodology was carefully followed to ensure that the corroded sample was perfectly cleaned from the corrosion products and the scales. This must be done to observe the surface directly exposed to the molten salt medium through the SEM, determining the type and the mechanism of the corrosion attack. For cross-sectional SEM analysis, the cross-section of the corroded sample, taken after the EIS test (no prior treatment on the corroded sample or de-scaling), was mounted in a cold-epoxy resin. The mounted sample was ground on 600, 1200 and 2400-grit silicon carbide papers, followed by polishing on 6, 1 and  $0.5 \mu\text{m}$  polishing pads. ISO/DIS 26146 standard was considered for metallographic examination of the samples after exposure to the molten salt medium [54]. The use of this standard was also mentioned by Firouzi and Shirvani [55]. Phase analysis of the corrosion products and the scales on the surface of the attacked specimens were studied by X-ray diffraction technique (XRD: Rigaku MultiFlex, Tokyo, Japan) and using Ni filtered Cu K $\alpha$  ( $\lambda_{\text{Cu K}\alpha} = 0.154186 \text{ nm}$ , radiation at 40 kV and 20 mA) over the 2 $\theta$  range of 10–80° (scan speed: 2° per minute, and step size: 0.04°). For phase analysis, the XRD patterns were compared to the standards compiled by the Joint Committee on Powder Diffraction and Standards (JCPDS) to identify the phases. The amounts of the dissolved alloying elements in the molten salt electrolyte were quantitatively measured using the ICP/AAS analysis.

## 3. Results and discussion

### 3.1. Microstructural study

Optical and SEM photomicrographs in Fig. 1 show the microstructure of the as-received wrought alloy 625. The mean grain size was  $10.23 \pm 2.63 \mu\text{m}$ . The chemical composition of the alloy can be

seen in Table 3. The alloy 625 exhibited the anisotropic microstructure including the annealed twin structures (Fig. 1a and b) after solid-solution treatment and the micron-sized carbides, distributed along the inter/intra-granular areas (Fig. 1c). EDX spectrum of the micron-sized carbides can be seen in Fig. 1d. These carbides are rich in niobium and titanium. From a physical metallurgy point of view, alloy 625 consists of a continuous FCC austenitic matrix (gamma phase:  $\gamma$ ) in which other phases reside, including  $\text{Ni}_3(\text{Al}, \text{Ti})$  intermetallic compound (gamma prime precipitate:  $\gamma'$ ) and carbides [56,57]. The gamma phase contains significant concentrations of chromium and molybdenum [58]. The gamma prime, which forms as a precipitate phase, often coherent with the  $\gamma$ -matrix, is rich in aluminum and titanium. Carbon, present in the wrought alloy 625 at 0.15 wt.% (Table 3), combines with titanium and/or niobium to form the micron-sized carbides which can be mainly found in the  $\gamma$ -grain boundaries (Fig. 1c and d). Inconel 625 is a solid solution alloy which is strengthened by precipitation of carbides such as  $\text{MC}$ ,  $\text{M}_6\text{C}$ , and  $\text{M}_{23}\text{C}_6$ , as well as intermetallic phases such as the  $\gamma$  phase [6,59].

### 3.2. DTA analysis

The simulated salt mixture in this research is a novel mixture composition, which has not been previously studied. The DTA curve of the prepared salt mixture can be seen in Fig. 2. A broad endothermic peak in the temperature range of 550–700 °C is distinguishable in the curve. This broad endothermic peak was caused by the heat adsorption due to the formation of the molten phase. There are no other obvious peaks in the DTA curve. Accordingly, the formation of the molten phase occurred in the temperature range of 550–700 °C. Also, the physical appearance and the visual monitoring of the salt mixture during the experiments at 600, 700 and 800 °C confirmed the presence of the molten phase at all the investigated temperatures.

### 3.3. OCP measurements

OCP curves of the alloy 625 at 600, 700 and 800 °C are presented in Fig. 3. At the beginning of the exposure, potential of the electrode increased, and then reached a steady value. The time ( $t_s$ ), which the electrode needed to reach the steady-state OCP and steady-state OCP of the electrode are mentioned in Fig. 3. At 700 and 800 °C, rapid increase in the potential of the electrode upon exposure to the molten salt is attributed to the spontaneous growth of an anodic film on surfaces of the electrode. The lowest  $t_s$  value occurs at 700 °C, which confirms the fastest growth rate of the anodic film at this temperature. Observed fluctuation in the OCP curves at the beginning of the exposure can be attributed to the unstable nature of the anodic film.

### 3.4. Potentiodynamic polarization study and weight-loss measurement

Fig. 4 shows potentiodynamic polarization curves of the alloy 625, exposed to the molten salt mixture at 600, 700 and 800 °C for 24 h, when the OCP reached a stable value. For the polarization curves in Fig. 4, it is not possible to apply the Tafel extrapolation technique to obtain the anodic and the cathodic Tafel slopes and the corrosion current density because a linear Tafel region, almost a decade of linearity, cannot be observed in the polarization curves, even in the cathodic branch of the curves. Consequently, calculation of the electrochemically measured corrosion rate is not possible. Potentiodynamic polarization curves are very useful to determine some corrosion mechanisms: active dissolution, passivation and pitting potentials, to name but a few. The alloy 625 exhibited the active dissolution behavior at all the investigated temperatures. The potentiodynamic polarization curves in Fig. 4

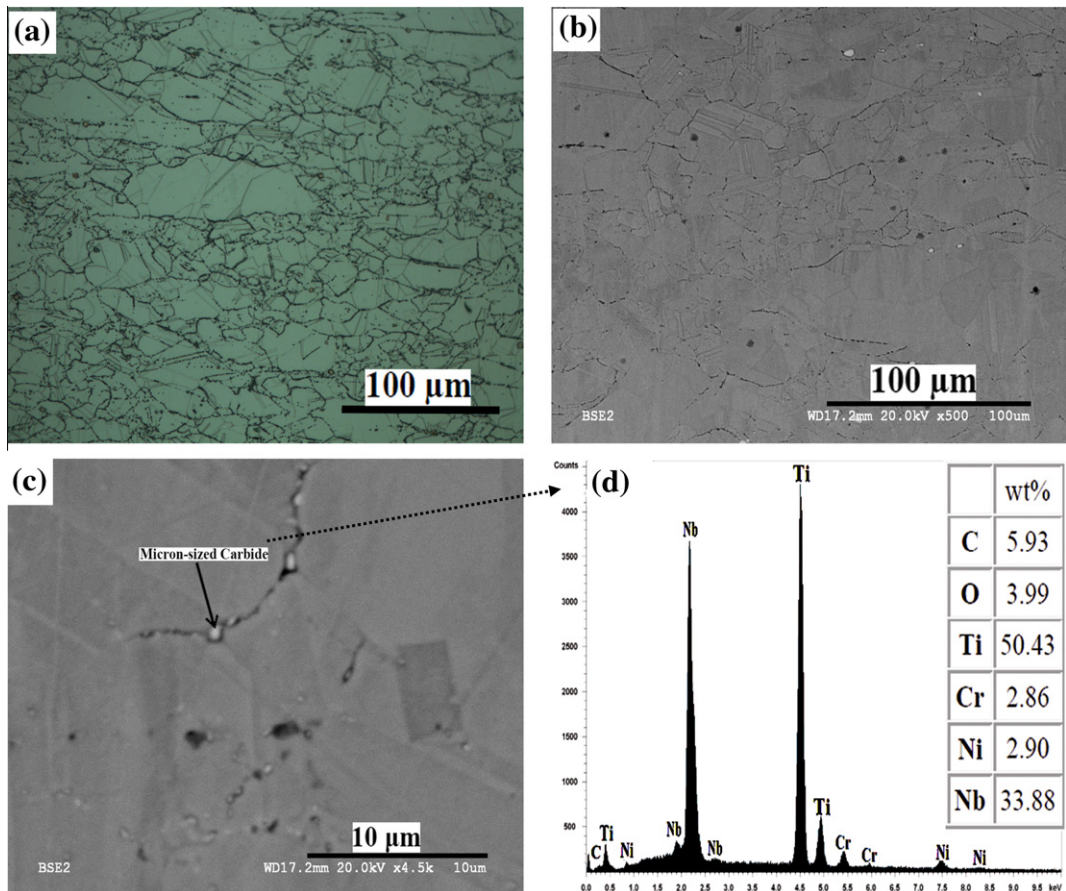


**Fig. 1.** Optical photomicrograph at (a) 500 times magnification and SEM photomicrographs (b and c) which show the microstructure of the wrought alloy 625, as well as (d) EDX spectrum of the micron-sized carbides.

**Table 3**

Chemical composition (wt.%) of the as-received wrought alloy 625.

Ni	Cr	Mo	Fe	Nb	Ti	Sb	Zn	Al	C	S	Si	Mn	Zr
55.08	20.97	8.30	4.50	2.80	0.16	0.20	0.25	0.44	0.15	0.02	0.31	0.05	0.01

are similar to those reported by Martínez-Villafañe et al. [60] for SAE213-T22 steel exposed to 80%  $V_2O_5$ -20%  $Na_2SO_4$  molten salt mixture, Espinosa-Medina et al. for Fe-40Al-0.1B-10Al<sub>2</sub>O<sub>3</sub> alloy exposed to  $NaVO_3$  molten salt at 700 °C [61] and Farrell and Stott [62]. Farrell and Stott explained that the shape of the curves is attributed to ohmic resistance of the molten salt. Despite the fact that molten salt is an ionic conductor, it can develop ohmic resistance due to dissolution of metal and metal oxides into the medium [62]. In the current study, the dissolution of the metal and the metal oxides into the molten salt medium was confirmed by XRD and ICP results (Section 3.7).

Based on the results of the potentiodynamic polarization test and the OCP measurement, the alloy 625 has the capability to form the anodic film at all the investigated temperatures in the molten salt medium. Morphology as well as chemical and phase analysis of the anodic films will be extensively discussed in Sections 3.5 and 3.7. At all the investigated temperatures, the anodic film is a non-protective layer/corrosion product film, which cannot provide an appropriate protection for the alloy against the corrosive medium. This is because the anodic current density increased rapidly when the potential shifted in the noble direction, exhibiting the

active dissolution behavior. Obviously, passivation of the alloy did not occur because the current densities are too high at all the investigated temperatures. According to Fig. 4, the potentiodynamic polarization curves show neither the passivation behavior nor a pitting potential, indicating that the alloy 625 is not susceptible to suffer from the pitting corrosion. Metal dissolution occurred by transport through a porous and non-protective oxide scale/anodic film. Formation of the non-protective porous anodic film was also confirmed by SEM and EIS results which will be discussed in Sections 3.5 and 3.6. Obtained corrosion potential ( $E_{corr}$ ) from the potentiodynamic polarization curves and the calculated corrosion rate from the Eq. (1), based on the weight-loss measurement technique, are presented in Table 4. By increasing the temperature, a rise in the mass fraction of the molten phase (Fig. 2) and mobility of electro-active species and ions caused the corrosion rate to increase.

### 3.5. SEM/EDX analysis

Fig. 5 shows morphology of the alloy 625 surfaces immediately after the EIS test in as-tested condition (Fig. 5a, c and e) and the

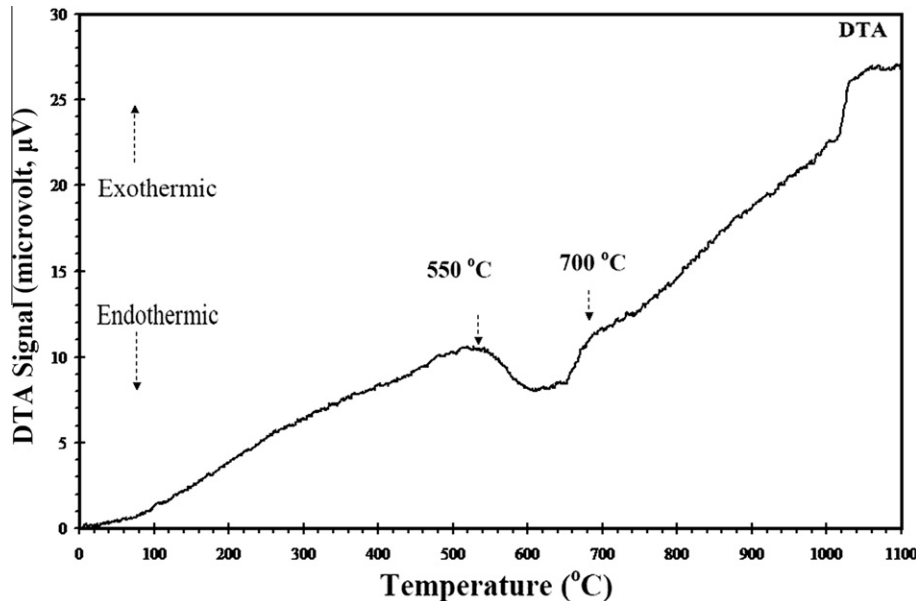
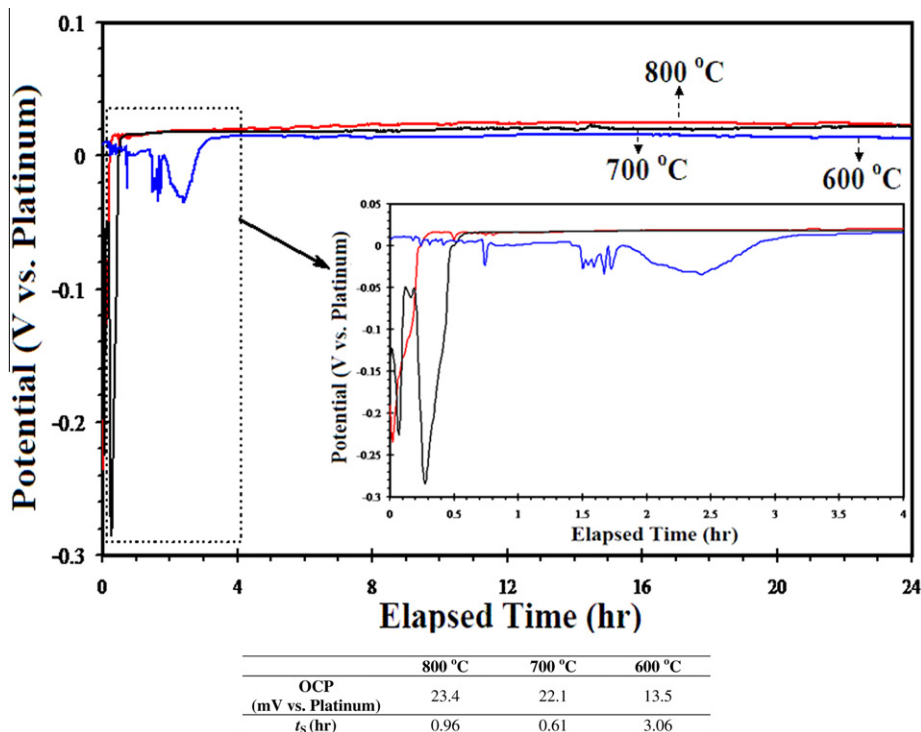
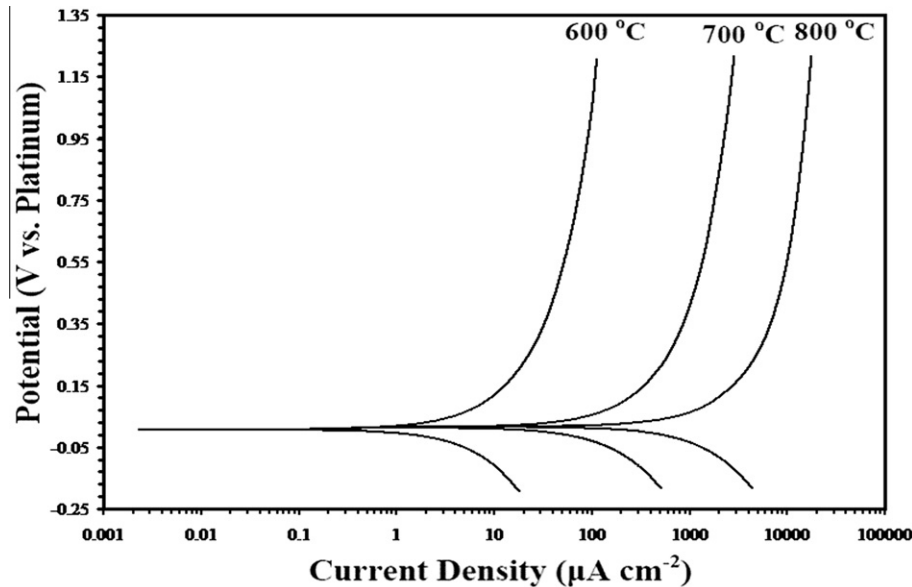


Fig. 2. DTA curve of the as-prepared simulated salt mixture.

Fig. 3. OCP of the alloy 625 electrode, exposed to the molten salt mixture at 600, 700 and 800 °C, as well as the time ( $t_s$ ) which the electrode needed to reach a steady-state OCP.

attacked surfaces (Fig. 5b, d and f), cleaned from the corrosion products and the scales. The cleaning procedure was based on the standard methodology presented in ASTM G1-03 [52]. It was necessary to clean the samples for observing the surfaces directly exposed to the molten salt medium. The corrosion products, a thick chromium-rich scale and lead-rich solidified salts can be seen in Fig. 5a, c, and e. Moreover, voids, a network of pores (internal attacked area) and intergranular attacked regions are clearly identifiable on the surface of the corroded alloy in Fig. 5b, d and f. Also, X-ray maps of oxygen, nickel, and chromium on the surface, as well as EDX elemental analysis (obtained through the cross-sectional

SEM study), are presented in Fig. 6 and Table 5, respectively, which show the elemental distribution, particularly for Cr, Ni, Nb, Mo, S and Cl, in the scale and the corroded surface of the alloy. According to the X-ray mapping results in Fig. 6 and EDX elemental analysis in Table 5, the corrosion product layer (anodic film/scale) mainly consists of chromium, oxygen, and nickel and no molybdenum was detected. Phase analysis of the scale will be discussed in Section 3.7. At 800 and 700 °C, underneath the chromium-rich corrosion product layer, there is a chromium-depleted zone, which is shown by a well-defined film of nickel-rich compound (Fig. 6) and it is also rich in oxygen. It confirms that the growth of the



**Fig. 4.** Potentiodynamic polarization curves of the alloy 625, exposed to the molten salt mixture at 600, 700 and 800 °C for 24 h.

**Table 4**

Obtained corrosion potential from the potentiodynamic polarization curves, and the calculated corrosion rate from the Eq. (1) for the alloy 625 samples, exposed to the molten salt mixture at 600, 700 and 800 °C for 24 h.

	800 °C	700 °C	600 °C
$E_{\text{corr}}$ (mV vs. Platinum)	16	13.5	7
Corr. rate (mm/year)	$26.54 \pm 1.69$	$14.25 \pm 2.01$	$1.80 \pm 0.33$

chromium-rich external scale was accompanied by the depletion of chromium within the subsurface region of the alloy. In the chromium-depleted zone, underneath the chromium-rich corrosion product layer, the concentration of chromium significantly decreases to 3.5, 9.5 and 11.5 wt.% for 800, 700 and 600 °C, respectively, which are considerably lower than the concentration of chromium in the wrought alloy 625 (the chromium content of the alloy 625: 20.97 wt.%, reported in Table 3). Accordingly, chromium is very prone to dissolution during the exposure of the alloy 625 to the molten salt (initiation stage) and the chromium-rich scale forms on the surface of the alloy (propagation stage). The concentration of chromium is almost the original composition of the alloy 625 underneath the chromium-depleted zone but the grain boundaries are rich in sulfur and oxygen in this region, which is shown in Fig. 9c and d. It should be noted that chromium is the most important alloying element, protecting the wrought alloy 625 against corrosive environments at ambient temperature through the formation of the protective chromium-nickel oxide,  $\text{Ni}(\text{Cr}_2\text{O}_4)$ , and  $\text{Cr}_2\text{O}_3$  layers as was confirmed by the XRD data (Fig. 12a).

SEM photomicrographs from the cross-section of the attacked alloy 625 immediately after the EIS test, can be seen in Fig. 7 at different magnifications. Also, Fig. 8 illustrates X-ray maps of oxygen, nickel, and chromium on the cross-section of the attacked alloy, as well as EDX elemental analysis of chromium, nickel, and oxygen in nickel- and chromium-rich layers. Based on the cross-sectional SEM images, mean thickness of the scale at 600, 700 and 800 °C was equal to  $5.59 \pm 2.33$ ,  $48.14 \pm 14.30$  and  $72.18 \pm 20.22 \mu\text{m}$ , respectively. Upon increasing the temperature, the thickness of the oxide layers and of the chromium-depleted zone rose. The porous and non-protective nature of the chromium-rich layer/scale is obvious in Figs. 7 and 8. Based on the SEM results in Figs. 5b, d and f as well as Fig. 7, general surface corrosion, intergranular corrosion,

formation of voids and a network of distributed pores on the surface and the cross-section, as well as internal oxidation (Fig. 8) and internal sulfidation (Fig. 9) were identified as different modes of corrosion attack. The high concentration of sulfur and oxygen in the grain boundaries are to blame for the occurrence of the intergranular corrosion together with the internal attack. Montgomery et al. [63] reported severe pitting and interdendritic (similar to the intergranular attack in the wrought alloy 625) corrosion of weld overlay alloy 625 at relatively low temperature of 300 °C in waste incinerator and biomass plants because of high presence of heavy metals together with chlorine; it was deduced that chloride and sulfates presented as heavy metal salts in melt or semi-melt phases, were responsible for pitting and interdendritic corrosion [63].

The chromium-rich corrosion product layer, which is highly porous and detached from the substrate particularly at 700 and 800 °C, shows the possible diffusion paths for the aggressive species (sulfur and oxygen) of the molten salt to reach the surface of the alloy and diffuse inward mainly through the grain boundaries. This is likely the main cause for the intergranular corrosion and the formation of the sulfur-oxygen rich regions (internal oxidation and sulfidation attack) in the internal attacked areas, as can be seen in Fig. 9. Fig. 8 confirms the selective oxidation of chromium in the internal attacked areas particularly at 700 and 800 °C. In fact, because of the non-protective and porous nature of the chromium-rich scale, the corrosive species diffused towards the alloy surface during the exposure of the alloy to the molten salt and it caused the intergranular corrosion process, which is exhibited in the internal attacked areas in Fig. 9, followed by the pores formation. The intergranular nature of the internal attacked area can be clearly observed in Fig. 9a, c, and d.

At the areas close to the interface of the alloy and the molten salt in the chromium-depleted zone, in addition to the intergranular attack, formation of the pores inside the grains is also evident (Fig. 9a). When the grain boundaries become rich in oxygen and sulfur at these areas, oxygen and sulfur diffuse into the grains; as a result, the internal attacked areas developed inside the grains. However, in Fig. 9c and d which belong to the areas located far enough from the surface of the alloy (underneath the chromium-depleted zone), the grains boundaries are rich in sulfur and oxygen, and the pores are at the early stage of development, initiating from the grain boundaries. Based on the EDX spectrum in Fig. 9b, the

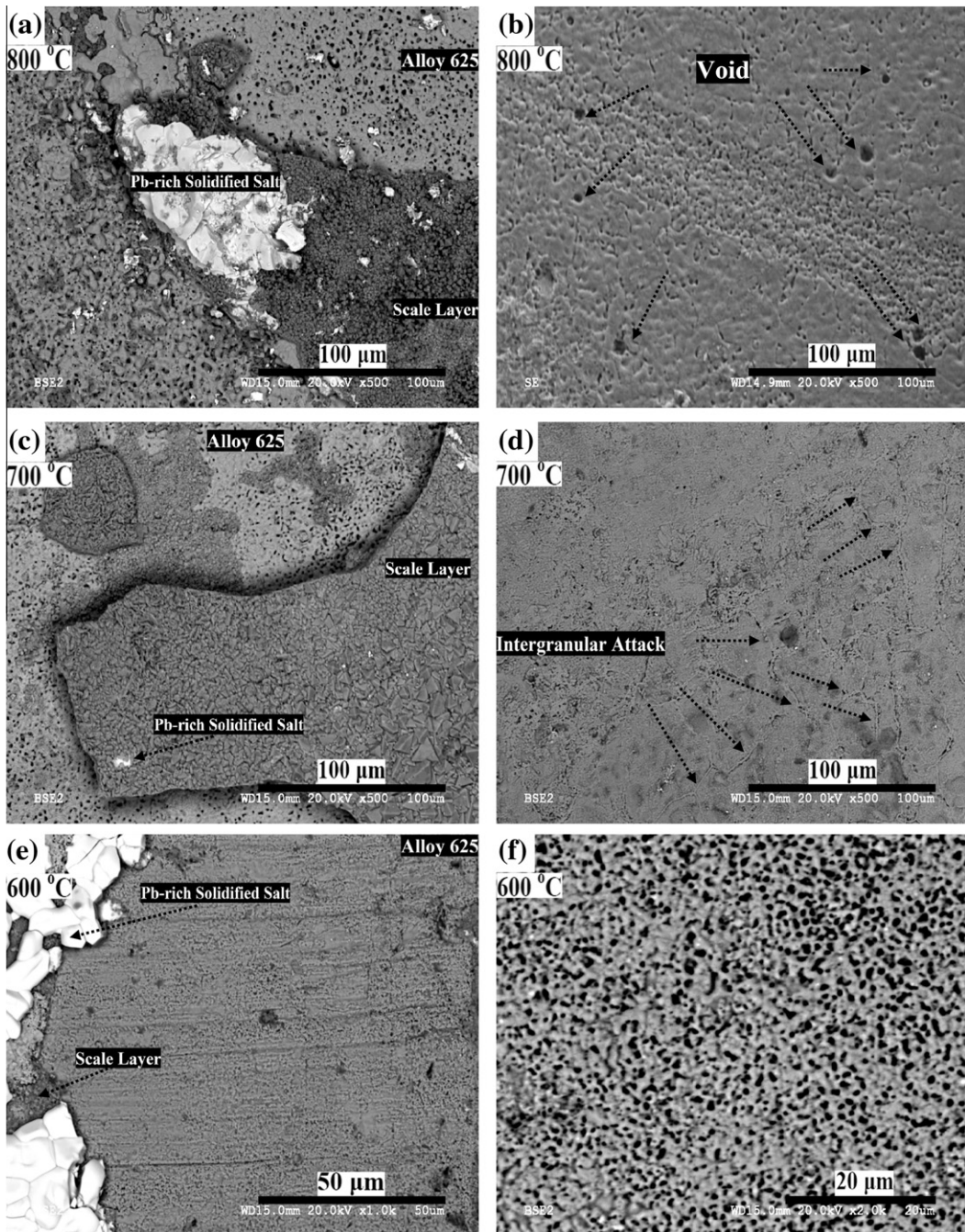


**Fig. 5.** SEM photomicrographs of surfaces of the alloy 625 corroded specimens immediately after the EIS test (a, c and e), which show morphology of scales and corrosion products, and attacked surfaces after cleaning and removing the corrosion products and the scales according to ASTM G1–03 (b, d and f).

amount of chromium in the sulfur-oxygen rich grain boundaries is very close to the chromium concentration in the wrought alloy 625 because these regions are located underneath the chromium-depleted zone and the depletion of chromium did not occur in this area. The fact of the matter is that the inward diffusion of oxygen and sulfur through the grain boundaries from the interface of the alloy and the molten salt is faster than the outward diffusion of chromium from the alloy, which caused the formation of the chromium-depleted zone and the development of the chromium-rich layer on the surface. For this reason, the diffusion depth of sulfur and oxygen through the grain boundaries is higher than the thickness of the chromium-depleted zone. As a result, underneath the chromium-depleted zone, there is an area with the chromium

concentration very close to the chemical composition of the wrought alloy 625 but the grain boundaries are rich in sulfur and oxygen in this area. In Fig. 9d, a few pores in the range of 70–200 nm in size, are shown at their early stage of formation. Moreover, the EDX analysis confirmed the presence of the niobium-rich regions in the grain boundaries, which contain 46.71 wt.% of niobium (Fig. 9e). The presence of the niobium-rich zones confirmed the tendency of niobium for migration to the grain boundaries from the bulk of the alloy during the internal oxidation/sulfidation phenomena. The migration of the niobium to the grain boundaries causes the galvanic effect between the niobium-rich zones in the grain boundaries region and the grain core, which can accelerate the formation of the pores.

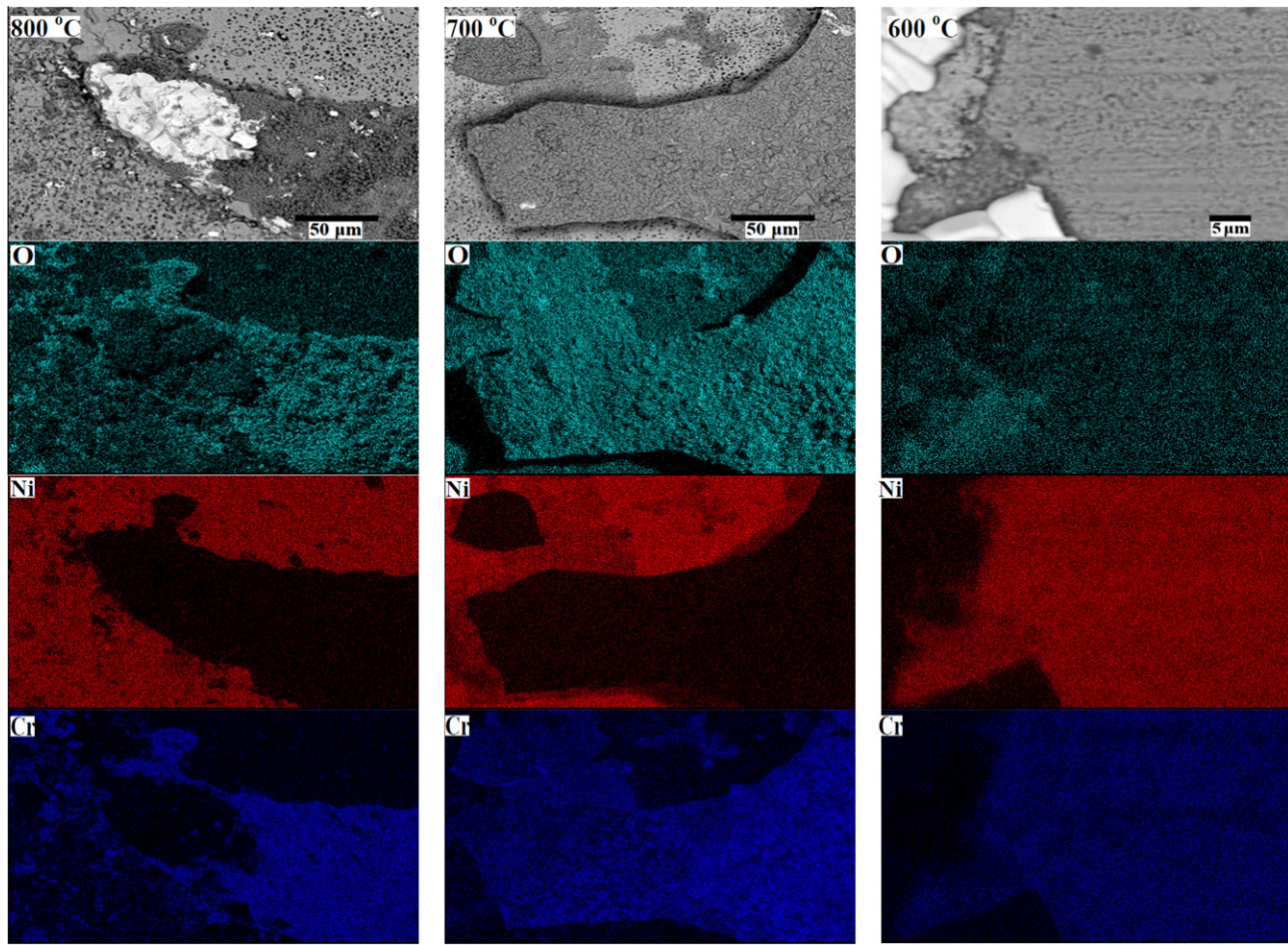


**Fig. 6.** X-ray mapping of oxygen, nickel and chromium on attacked surface of the alloy 625, exposed to the molten salt mixture for 24 h.

**Table 5**  
EDX elemental analysis (wt.%) from the attacked surface of the alloy 625 corroded samples, exposed to the molten salt mixture for 24 h.

	Attacked surface of alloy 625			Outer surface of scale		
	800 °C	700 °C	600 °C	800 °C	700 °C	600 °C
Ni	54.80 ± 1.46	54.48 ± 3.28	59.11 ± 0.2	19.67 ± 3.53	7.42 ± 0.73	20.49 ± 2.41
Cr	3.55 ± 0.81	9.57 ± 2.2	11.56 ± 0.69	14.22 ± 1.08	43.69 ± 1.91	24.18 ± 1.70
Mo	8.37 ± 1.04	8.6 ± 0.63	8.6 ± 0.41	ND	ND	ND
Nb	2.24 ± 0.32	0.54 ± 0.16	1.24 ± 0.13	1.09 ± 0.17	2.76 ± 0.03	2.24 ± 0.24
Ti	0.1 ± 0.01	0.11 ± 0.03	0.09 ± 0.02	0.15 ± 0.01	0.34 ± 0.01	0.33 ± 0.06
O	17.83 ± 1.39	16.41 ± 4.32	10.3 ± 0.45	32.6 ± 4.68	31.06 ± 0.64	28.70 ± 1.00
Fe	2.98 ± 0.26	1.07 ± 0.47	2.58 ± 0.16	3.3 ± 0.54	0.19 ± 0.01	10.1 ± 0.71
Al	0.1 ± 0.01	0.1 ± 0.02	0.1	0.89 ± 0.20	0.22 ± 0.08	0.6 ± 0.24
Si	0.25 ± 0.05	0.37 ± 0.08	0.3 ± 0.04	3.68 ± 0.35	0.42 ± 0.13	0.89 ± 0.1
Cl	0.15 ± 0.03	1.16 ± 0.1	0.12 ± 0.04	ND	0.11 ± 0.1	0.14 ± 0.03
S	ND	ND	ND	0.33 ± 0.06	3.86 ± 1.06	0.85 ± 0.20
Zn	ND	ND	ND	13.84 ± 2.84	ND	4.95 ± 0.21
Pb	ND	ND	ND	2.05 ± 1.1	ND	1.37 ± 0.17
C	8.67 ± 0.38	7.48 ± 1.97	6.05 ± 0.75	8.3 ± 0.4	5.39 ± 0.28	4.41 ± 0.23

(ND: Not Detected).

With regard to the occurrence of the internal oxidation, when chromium is selectively oxidized, particularly in the grain boundaries which act as the fast diffusion paths for the oxygen and sulfur diffusion, but cannot reach the surface quickly enough to develop a scale, the internal oxidation occurs. Initiation of the internal attack begins from the grain boundaries because activation energy for grain boundary diffusion is generally only about half that for volume diffusion [64]. Furthermore, it has been clearly established that alloy grain boundaries act as preferential paths for sulfur

diffusion over a wide range of temperature leading to precipitation of sulfide in intergranular regions and consequently occurrence of internal sulfidation [65]. According to the SEM results, the internal oxidation of chromium and the external scaling occurred. Obviously, with increasing the temperature, the depth of the chromium-depleted zones and the thickness of the internal attacked area increased due to the kinetic effect (Fig. 8). In WTE boiler environments, when the molten phase contained chlorine and sulfur, corrosion products of alloy 625 had lamellar structures

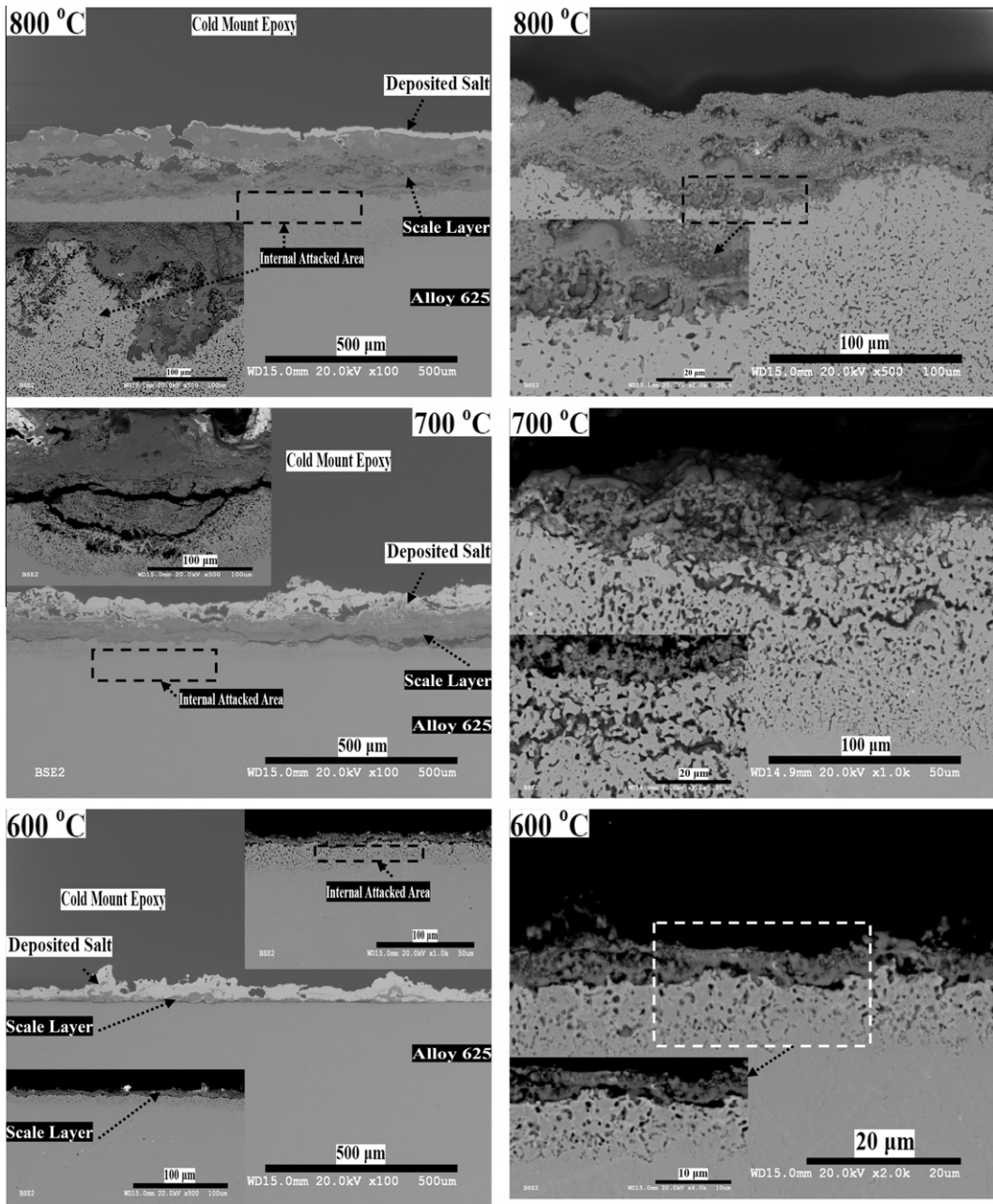


**Fig. 7.** Cross-sectional SEM photomicrographs of the attacked alloy 625 samples, exposed to the molten salt mixture for 24 h.

and occurrence of oxidation, sulfidation, and chlorination was confirmed at the alloy/scale interface under a low partial pressure ( $P$ ) of oxygen ( $P_{O_2}$ )-high  $P_{Cl_2}$  condition [29].

Reportedly, a significant percentage of high-temperature corrosion failure involves internal oxidation [66]. The internally precipitated reaction products cause embrittlement and dilation of alloy subsurface region, which can cause affected zone to flake off. Because the process is supported by diffusion of interstitial species (for example dissolved oxygen and sulfur in the current study), it is rapid and the internal oxidation is known as a very destructive process in industrial applications [66].

During the initiation stage of hot corrosion, alloy and deposit face with some changes including: (1) depletion of elements which are responsible for formation of protective scale on the alloy's surface (mainly chromium in alloy 625), (2) incorporation of sulfur

from deposit into the alloy and, (3) dissolution of oxides into the salt and development of cracks or channels into the scale. These are to blame for making the alloy susceptible to rapid corrosion attack and degradation at the second stage of hot corrosion (propagation stage). Local penetration of the molten salt through the scale and subsequent spreading along the scale/alloy interface can occur at the end of the initiation stage. As a result, the molten salt can reach the sites with low oxygen activity and chromium-depletion when alloy is a nickel-based superalloy containing high percentage of chromium, facilitating a rapid propagation stage. At the initiation stage of hot corrosion, oxidation of alloying elements, mainly chromium, nickel, and niobium in the current study (Table 5), causes the electron transfer from the metallic atoms to the medium. By starting the second stage of hot corrosion (propagation stage), protective nature of oxide scales drastically alters

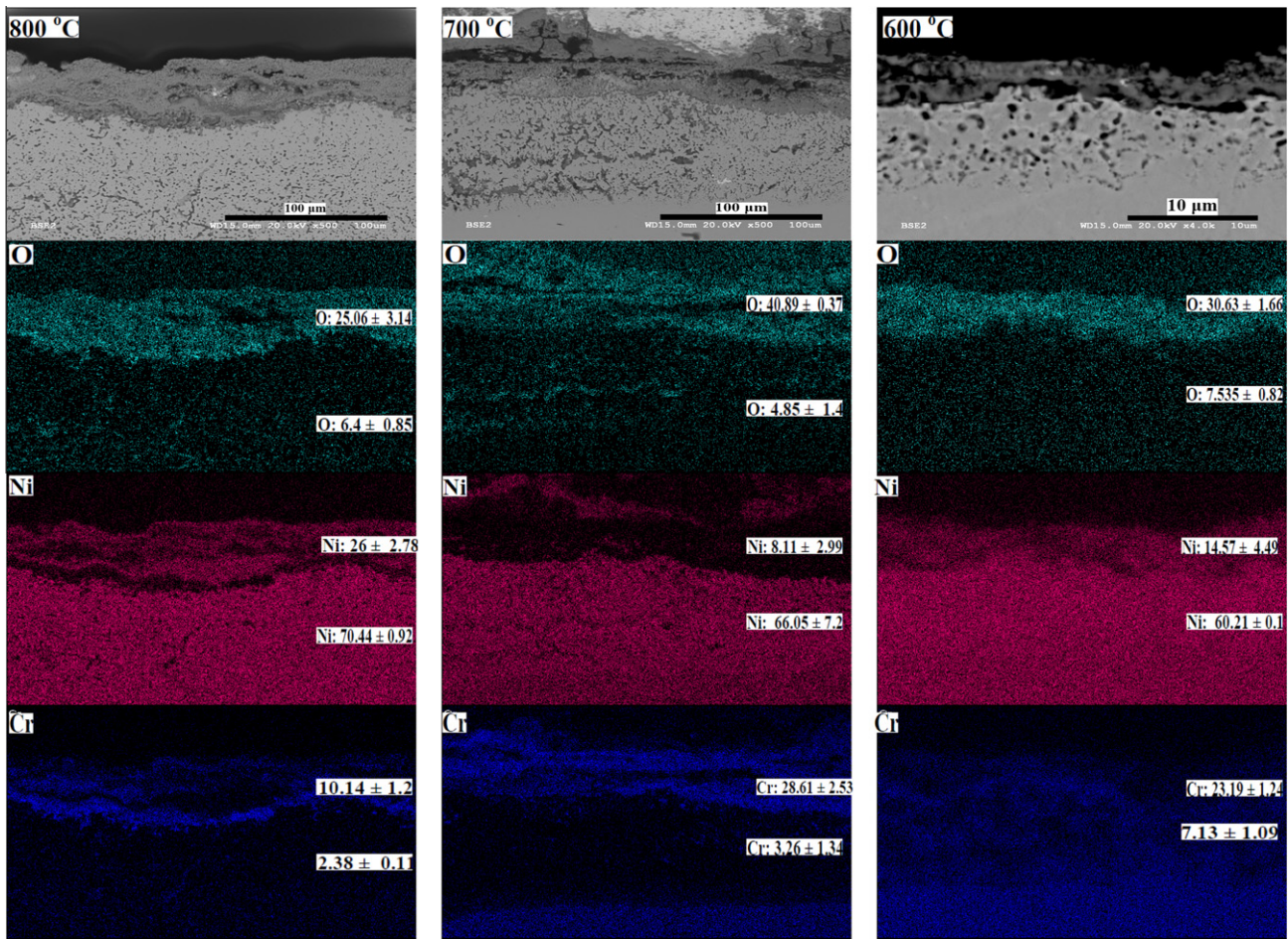


**Fig. 8.** X-ray mapping of oxygen, nickel and chromium on the cross-section of the attacked alloy 625 samples, exposed to the molten salt mixture for 24 h, and EDX elemental analysis of nickel, chromium and oxygen in chromium- and nickel-rich layers.

because the oxide scales become porous and non-protective and subsequently the alloy experiences a rapid corrosion [28,67–70].

### 3.6. EIS study

The impedance behavior of the alloy 625 electrode including the measured and the calculated Nyquist plots plus the Bode diagrams of the phase angle and the total impedance magnitude at 600, 700 and 800 °C, are presented in Fig. 10. Considering the extensive discussion in the Section 3.5 on the surface and the cross-sectional properties of the alloy 625 after 24 h exposure to the molten salt medium, the EIS data were fit into two equivalent circuits, representing a porous and non-protective scale model. The model parameters for the equivalent circuits can be seen in Fig. 11. The Nyquist diagrams show two depressed capacitive loops, including a loop at high frequency, relatively large at 700 and 600 °C, and a loop at low frequency range, relatively large at 800 °C. The capacitive loop, which is related to the dielectric properties of the chromium-rich scale, located at 50 kHz–1.15 mHz, 4340 Hz–39.2 mHz, and 50 kHz–832 mHz frequency range at 600, 700 and 800 °C, respectively. Based on the presented model parameters for the equivalent circuits in Fig. 11, the charge transfer resistance of the outer chromium-rich barrier layer ( $R_{sl}$ ) is relatively low at 700 and 800 °C. Consequently, the barrier layer did not act as an effective protective layer, as was confirmed by the SEM, the potentiodynamic polarization and the weight-loss measurement results. In fact, the barrier layer can be considered as a corrosion

product, not an effective protective layer. In the Nyquist plots of Fig. 10, the values of both real and imaginary impedance rose with decreasing the temperature to 600 °C, resulting in an increase in the impedance modulus and the radius of the capacitive loop. At 600 and 700 °C, the corresponding curves of the phase angle vs. frequency have one relatively symmetrical maximum at 1.53 Hz and 832 mHz, respectively. Also, a shoulder, which has a maximum at 5.2 Hz, is identifiable in the phase angle vs. frequency curve of 800 °C. These relaxation processes are related to the growth of the porous scale.

According to the suggested equivalent circuits, the capacitive loop at higher frequencies (600 °C: 50 kHz–1.15 mHz; 700 °C: 4340 Hz–39.2 mHz; and 800 °C: 50 kHz–832 mHz) is attributed to the dielectric properties of the scale, formed on the electrode surface from which the chromium-rich layer resistance value ( $R_{sl}$ : transfer resistance of ions in the scale) is determined.  $Q_{dl}$  and  $R_{dl}$  represent the double-layer capacitance and the charge transfer resistance along the pores in the porous scale. Also,  $Q_{sl}$  ( $C_{sl}$  at 600 °C) is the representation of the capacitive behavior of the scale. Constant phase element (CPE) is utilized to account for non-uniform current distribution from the pure capacitive behavior and the deviation due to surface inconsistencies. By increasing the temperature from 600 to 700 and 800 °C, the value of  $R_s$  (solution resistance between the working and the reference electrode) decreased because viscosity of the molten salt reduced as a result of an increase in the temperature, while the mass fraction of the molten phase increased, simultaneously, based on the DTA curve in

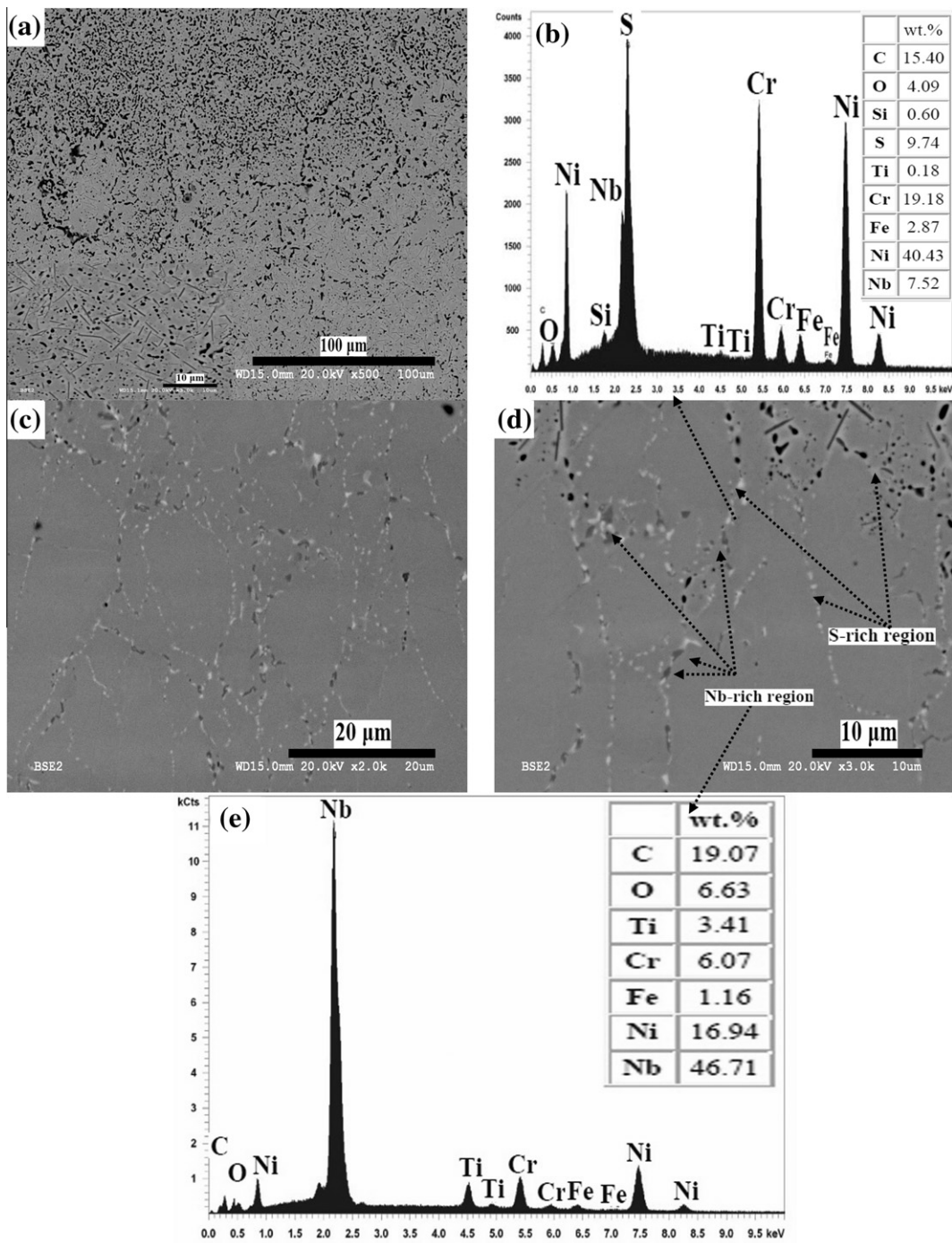


**Fig. 9.** SEM photomicrographs of the alloy 625 cross-section, exposed to the molten salt mixture for 24 h at 800 °C, which show the (a) intergranular nature of the oxidation in the internal attacked areas, (c and d) sulfur/nickel-rich grain boundaries underneath the chromium-depleted zone as well as (b) EDX spectrum of the white regions, and (e) EDX spectrum of the niobium-rich regions in the grain boundaries.

**Fig. 2.** These two factors enhanced the diffusion of the aggressive species from the molten medium toward the interface of the molten phase/electrode surface and subsequently accelerated the corrosion of the alloy. A straight line, slope smaller than  $-1$  at high frequency range of 50 kHz–4340 Hz, is distinguishable in the Bode diagram at 700 °C. This feature is related to frequency dispersion and can be attributed to solid surface inhomogeneities [71]. At all the investigated temperatures, the phase angle maxima were much smaller than 90°. Carranza and Alvarez explained that surface roughness, frequency dispersion of time constants due to local

inhomogeneities in dielectric material, porosity mass transport effects and relaxation effects are some reasons of this phenomenon [72]. In the current study, the main reasons for having phase angles much smaller than 90° are the porosity mass transport effects and the frequency dispersion of the time constants due to local inhomogeneities in the dielectric material. It looks that the latter is due to the inhomogeneous nature of the molten salt mixture. As a result, a constant phase element (CPE) was introduced into the equivalent circuits, proposed to reproduce the results, to account for these effects.

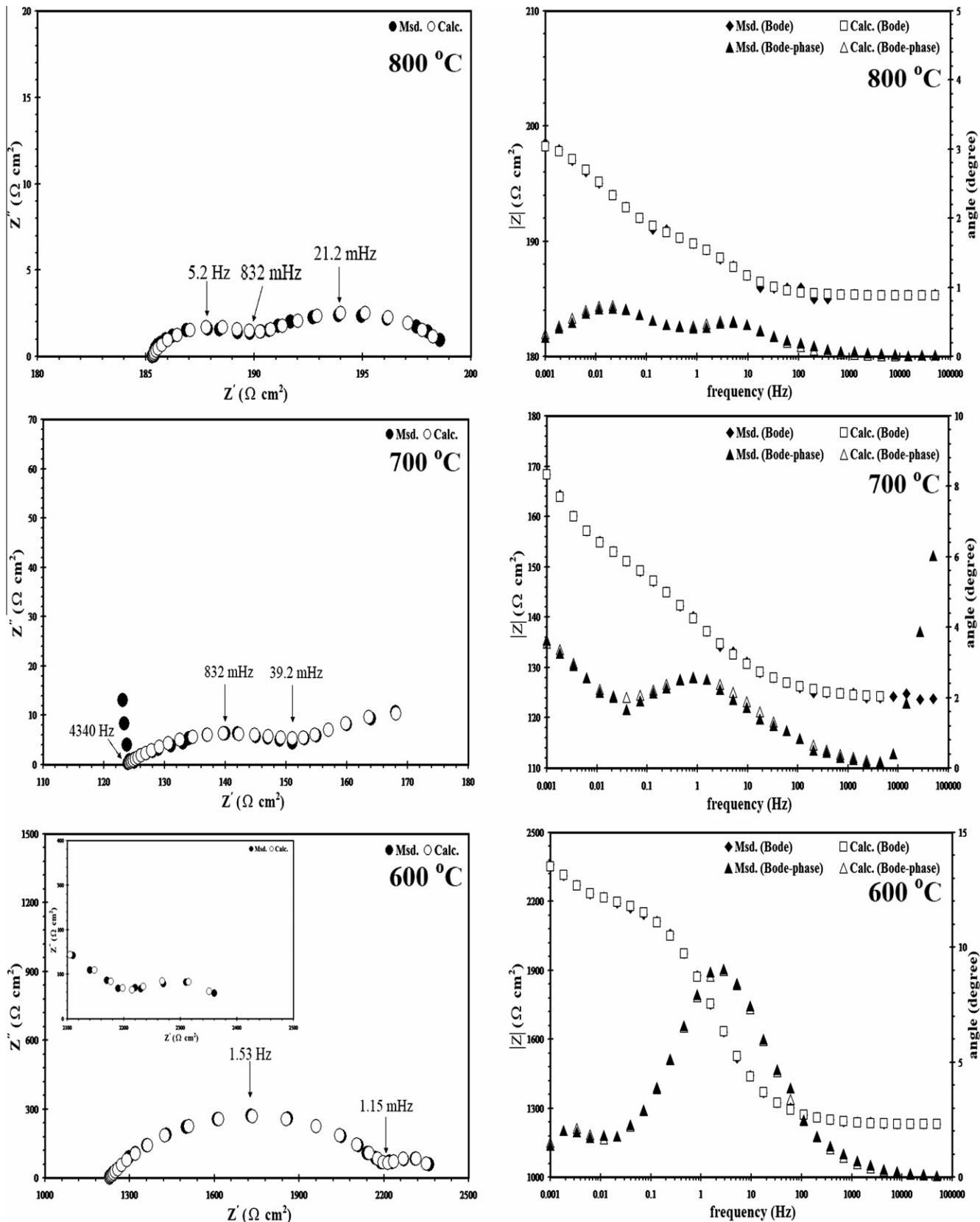


**Fig. 10.** Electrochemical impedance spectroscopy (EIS) Nyquist plots response plus Bode diagrams of phase angle and total impedance magnitude for the alloy 625, exposed to the molten salt mixture for 24 h.

Beverskog et al. mentioned that the number of distinguishable maxima or related shoulders was an indication of the minimum number of relaxation processes (time constants) that occurred in

electrochemical system, which were detectable thorough EIS [73]. A porous scale model was suggested by Perez et al. [74] to explain the corrosion of alloy 625 beneath molten  $ZnCl_2-KCl$  mixture

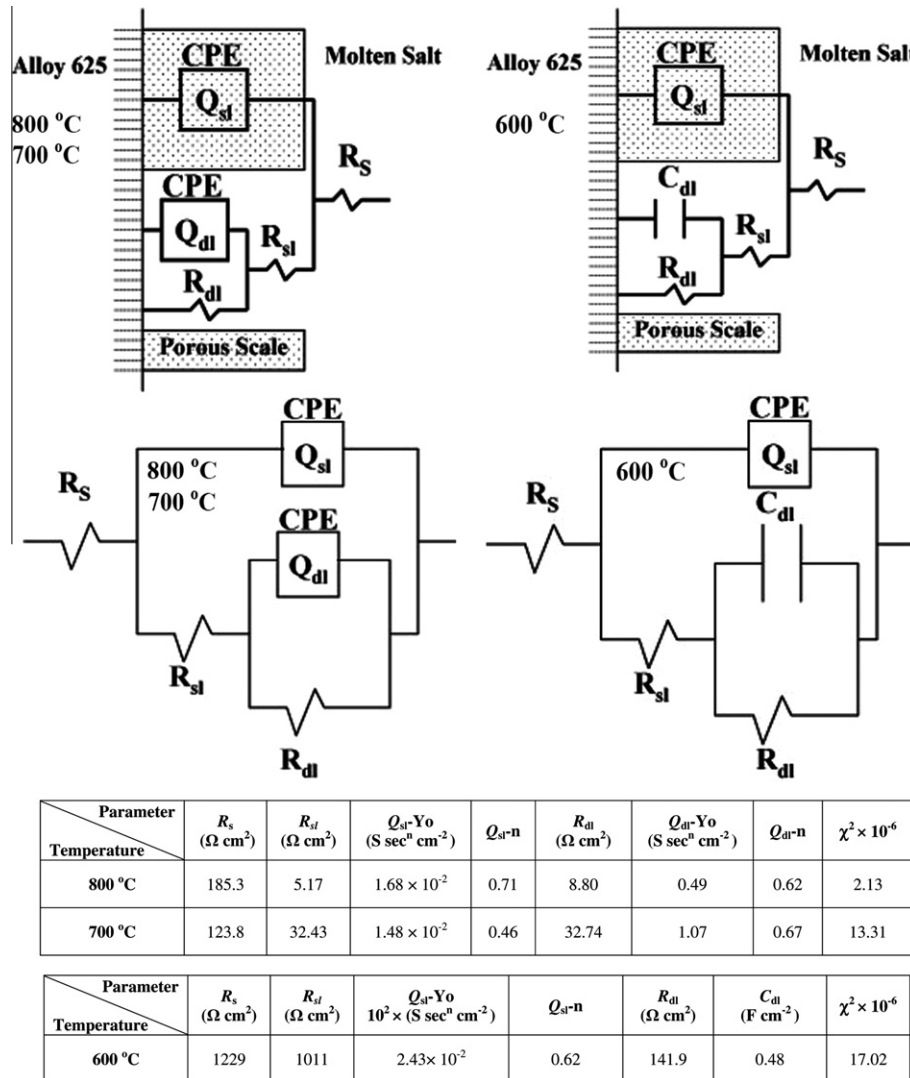


**Fig. 11.** Equivalent electrochemical circuits (porous and non-protective scale model) plus the model's parameters of the equivalent circuits for the alloy 625, exposed to the molten salt mixture for 24 h.

at 650 °C after 100 h exposure. In this case, corrosion mechanism was controlled by diffusion of aggressive ions through alloy/melt interface and EIS profiles were fit to a protective scale model before 100 h exposure [74,75].

### 3.7. XRD analysis

After exposing the alloy to the molten salt for 24 h, the surfaces of the samples were covered by a thick layer of corrosion products (Figs. 5 and 7) and the scales. In order to identify these corrosion products and the scales, formed on the surface of the alloy after the EIS test, the surfaces of the corroded specimens were studied by XRD technique. The XRD patterns of the as-received alloy 625 surface and the initial salts, in comparison with the prepared simulated salt mixture, are presented in Fig. 12a and b. The XRD patterns of the attacked surface of the specimens, in comparison with the standard XRD patterns (JCPDS file) of the major identified phases, at 800, 700 and 600 °C (after the EIS test) can be seen in Figs. 13–15, respectively. Also, list of the corrosion products extracted from the XRD patterns in Figs. 13–15, is presented in Table 6. In order to identify the observed peaks in the XRD patterns, the obtained XRD patterns compared with the standard

JCPDS cards of almost 9000 phases, which were selected based on the available elements in the molten salt/alloy system. Fig. 12a confirms that the protective layer of the wrought alloy 625 consists of Ni(Cr<sub>2</sub>O<sub>4</sub>) (JCPDS # 01-089-6615) and Cr<sub>2</sub>O<sub>3</sub> (JCPDS # 01-04-0315) phases at ambient temperature. However, the characteristic peaks of the Ni(Cr<sub>2</sub>O<sub>4</sub>) and the Cr<sub>2</sub>O<sub>3</sub> protective layers completely disappeared/dissolved when the alloy exposed to the molten salt medium at 600, 700 and 800 °C. The dissolution of the protective layers justifies weak corrosion resistance/appreciable corrosion susceptibility of the alloy 625 in the molten salt medium as was previously confirmed by the potentiodynamic polarization test and the weigh-loss measurement (Section 3.4). Nickel, chromium, iron, niobium, and titanium alloying elements in the chemical composition of the alloy 625 have tendency to dissolution in the molten salt.

Based on the XRD results, nickel mainly dissolved in the molten salt as Ni<sup>2+</sup> at 800 and 600 °C. According to Table 6, the dissolution of chromium in the form of Cr<sub>5</sub>S<sub>6</sub> at 800 °C, Cr<sup>2+</sup> at 700 °C and CrO<sub>4</sub><sup>2-</sup> at 600 °C caused the breakdown and the degradation of the protective layer. Weak characteristic peaks of NiCr<sub>2</sub>O<sub>4</sub> are identifiable in the XRD pattern at 600 °C (Fig. 15). The NiCr<sub>2</sub>O<sub>4</sub> phase was characterized as a porous layer, based on the SEM results in

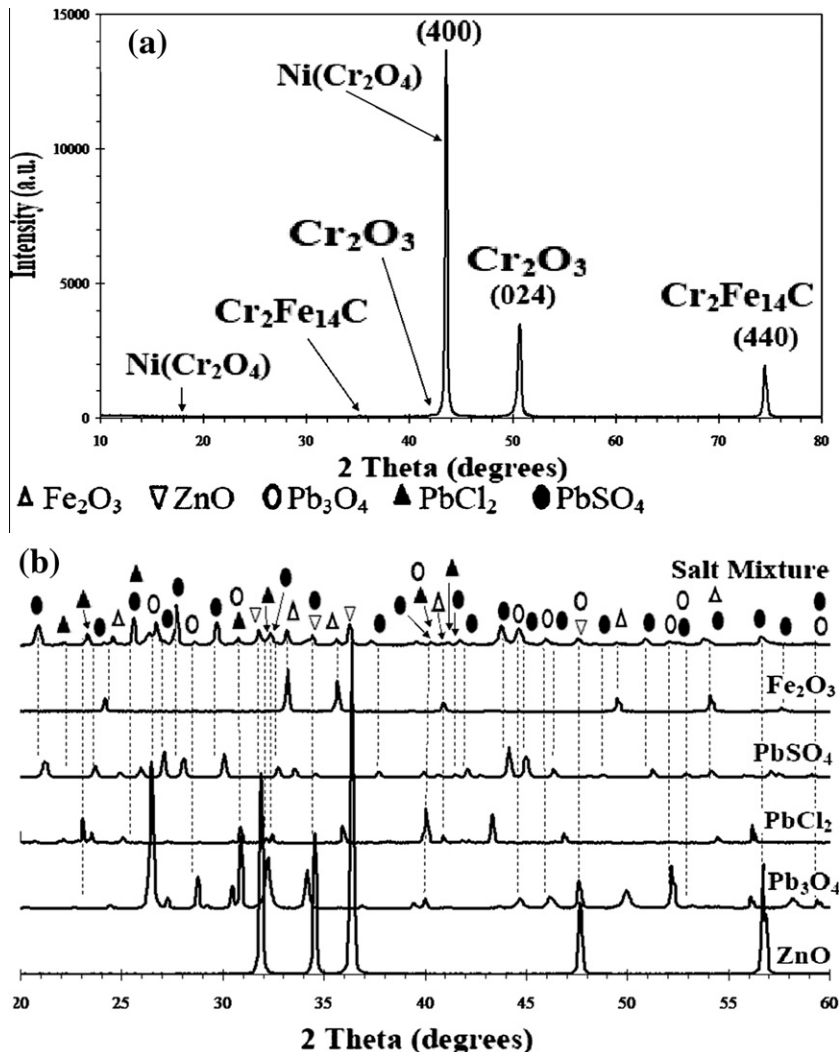


**Fig. 12.** X-ray diffraction (XRD) patterns of (a) surface of the as-received wrought alloy 625 after polishing and (b) the initial salts and the prepared simulated salt mixture.

Figs. 7 and 8. Consequently, the NiCr<sub>2</sub>O<sub>4</sub> layer cannot act as an effective protective layer. Molybdenum showed a strong resistance to dissolution in the molten salt at 600 and 700 °C, while it was dissolved in the form of Fe(MoO<sub>4</sub>) at 800 °C. The concentration of the dissolved molybdenum in the molten salt mixture, measured by means of ICP technique, was equal to 153, 38 and 6 ppm at 800, 700 and 600 °C, respectively. The amounts of the dissolved chromium and nickel in the molten salt mixture were determined as: Ni, 75, 26 and 11 ppm at 800, 700 and 600 °C, respectively; and Cr, 630, 209 and 14 at 800, 700 and 600 °C, respectively.

Formation of CrNbO<sub>4</sub> in scale was reported by Perez et al. during degradation of alloy 625 in ZnCl<sub>2</sub>-KCl molten salt mixture at 650 °C [74]. Ishitsuka et al. [76] reported that fast dissolution of Cr<sub>2</sub>O<sub>3</sub> happened and chromium dissolved as a hexavalent chromium ion in molten chloride and chloride/sulfate mixture. In fact, in the molten chloride environments, which mainly formed in WTE boilers, the dissolution of the protective Cr<sub>2</sub>O<sub>3</sub> films could occur through the chemical formation of CrO<sub>4</sub><sup>2-</sup> [76]. In the current study, the dissolution of chromium in the form of CrO<sub>4</sub><sup>2-</sup> occurred at 600 °C (Fig. 15 and Table 6). In the presence of molybdenum, vanadium or tungsten in the alloy, since these elements have a tendency to form their oxides on the surface of the alloy, P<sub>O<sub>2</sub></sub> of the molten salt at the interface will increase and the solubility of Cr<sub>2</sub>O<sub>3</sub> will be expected to decrease [77]. Therefore, these protective

oxide films can effectively assist the Cr<sub>2</sub>O<sub>3</sub> layer to protect the alloy against the corrosive molten salt containing chlorine ions [77]. Obviously, these oxides could protect the substrate from the hot corrosion if they demonstrate a low solubility in a molten salt corrosive environment, which is a somewhat basic solution especially in WTE boilers. Despite the fact that Fe<sub>2</sub>O<sub>4</sub> is another oxide having low solubility in such a corrosive environment, it could not play the role of a protective oxide layer because of weak protective properties [18].

### 3.8. Platinum electrodes stability

ICP/AAS was used to analyze the elemental composition of the molten salt electrolyte after the electrochemical tests at 600, 700 and 800 °C. Platinum element was not detected by ICP/AAS in the chemical composition of the molten salt electrolyte. This confirms that platinum reference and counter electrodes do not react with the molten salt during the electrochemical tests and no degradation of the platinum electrode in the molten salt medium occurs. Furthermore, phase composition of the platinum wires, in as-received condition and after exposure to the molten salt during the electrochemical tests, was studied by XRD technique and results can be seen in Fig. 16. Both patterns illustrate only the characteristic peaks of platinum (JCPDS # 00-004-0802) and no differences

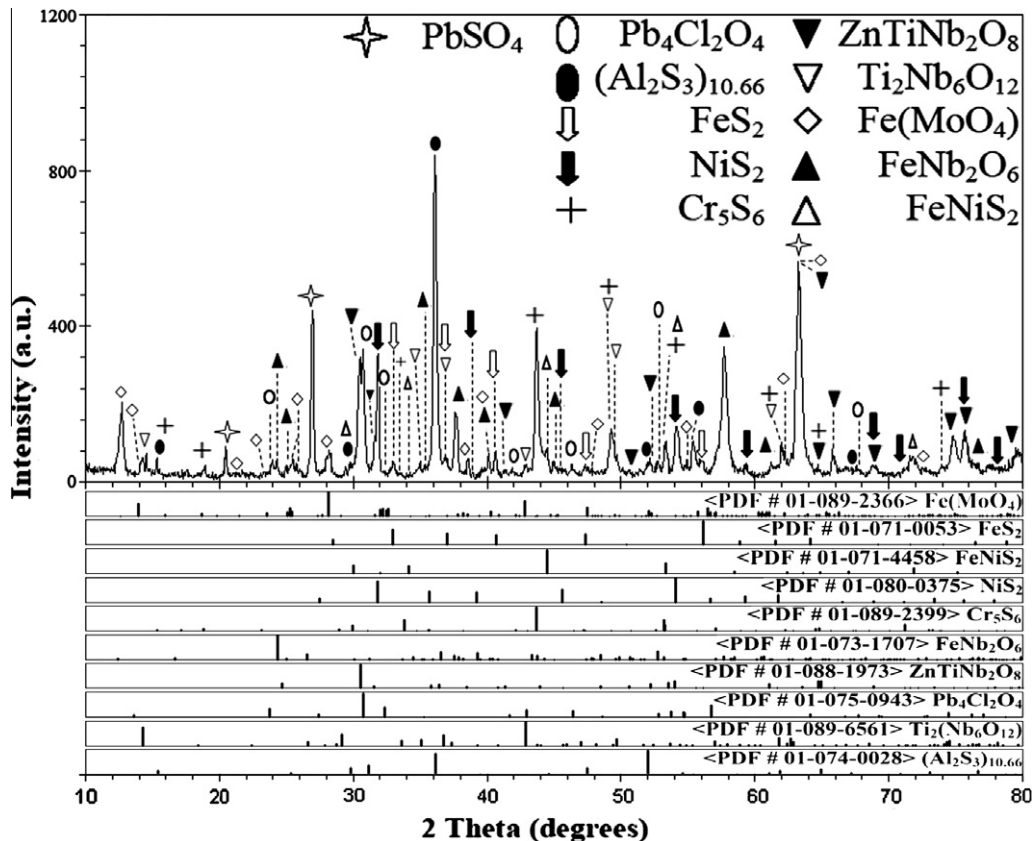


**Fig. 13.** X-ray diffraction (XRD) pattern of attacked surface of the alloy 625 after the EIS test at 800 °C in comparison with the standard XRD patterns of the identified components, compiled by JCPDS.

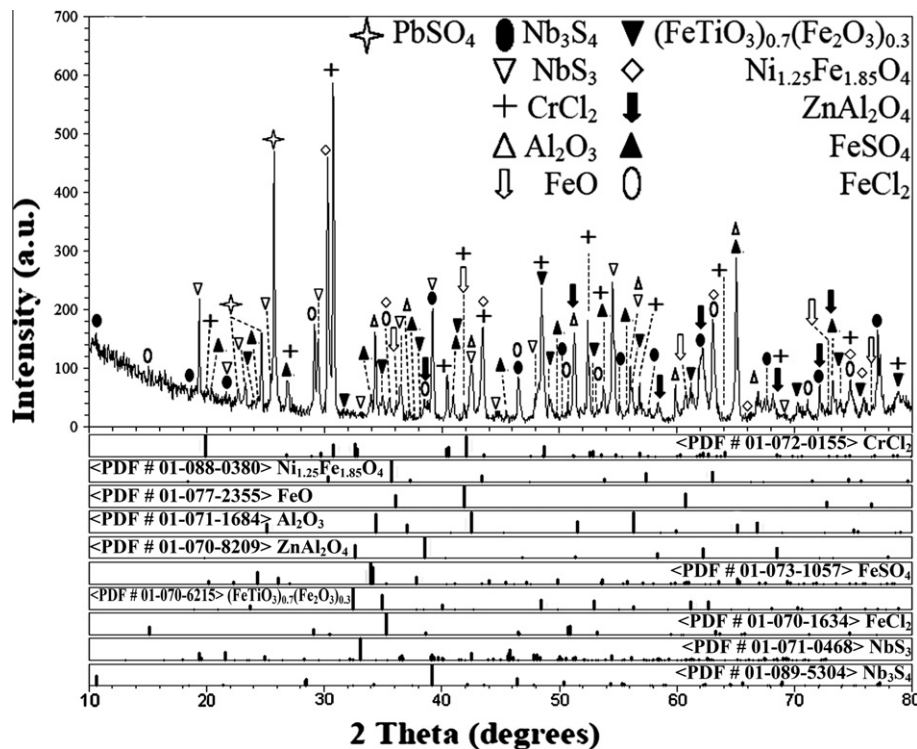


**Fig. 14.** X-ray diffraction (XRD) pattern of attacked surface of the alloy 625 after the EIS test at 700 °C in comparison with the standard XRD patterns of the identified components, compiled by JCPDS.

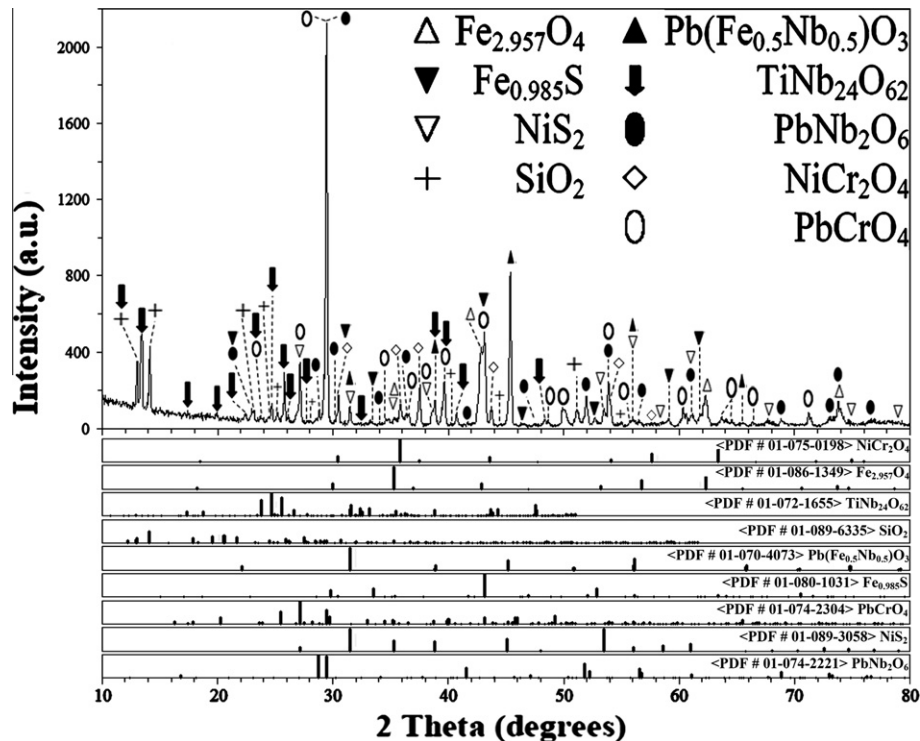


**Fig. 15.** X-ray diffraction (XRD) pattern of attacked surface of the alloy 625 after the EIS test at 600 °C in comparison with the standard XRD patterns of the identified components, compiled by JCPDS.

**Table 6**

Identified corrosion products, in the phase structure of the scales, extracted from Fig. 13–15.

Temperature element	800 °C	700 °C	600 °C
Ni	$\text{NiS}_2$ , $\text{FeNiS}_2$	$\text{Ni}_{1.25}\text{Fe}_{1.85}\text{O}_4$	$\text{NiS}_2$ , $\text{NiCr}_2\text{O}_4$
Cr	$\text{Cr}_5\text{S}_6$	$\text{CrCl}_2$	$\text{PbCrO}_4$ , $\text{NiCr}_2\text{O}_4$
Mo	$\text{Fe}(\text{MoO}_4)$	–	–
Fe	$\text{Fe}_2\text{S}_2$ , $\text{FeNiS}_2$ , $\text{FeNb}_2\text{O}_6$ , $\text{Fe}(\text{MoO}_4)$	$\text{FeO}$ , $\text{FeSO}_4$ , $\text{FeCl}_2$ , $\text{Ni}_{1.25}\text{Fe}_{1.85}\text{O}_4$ ( $\text{FeTiO}_3$ ) <sub>0.7</sub> ( $\text{Fe}_2\text{O}_3$ ) <sub>0.3</sub>	$\text{Fe}_{0.985}\text{S}$ , $\text{Pb}(\text{Fe}_{0.5}\text{Nb}_{0.5})\text{O}_3$ , $\text{Fe}_{2.975}\text{O}_4$
Nb	$\text{ZnTiNb}_2\text{O}_8$ , $\text{FeNb}_2\text{O}_6$ , $\text{Ti}_2(\text{Nb}_6\text{O}_{12})$	$\text{NbS}_3$ , $\text{Nb}_3\text{S}_4$	$\text{PbNb}_2\text{O}_6$ , $\text{TiNb}_{24}\text{O}_{62}$ , $\text{Pb}(\text{Fe}_{0.5}\text{Nb}_{0.5})\text{O}_3$
Ti	$\text{ZnTiNb}_2\text{O}_8$ , $\text{Ti}_2(\text{Nb}_6\text{O}_{12})$	( $\text{FeTiO}_3$ ) <sub>0.7</sub> ( $\text{Fe}_2\text{O}_3$ ) <sub>0.3</sub>	$\text{TiNb}_{24}\text{O}_{62}$

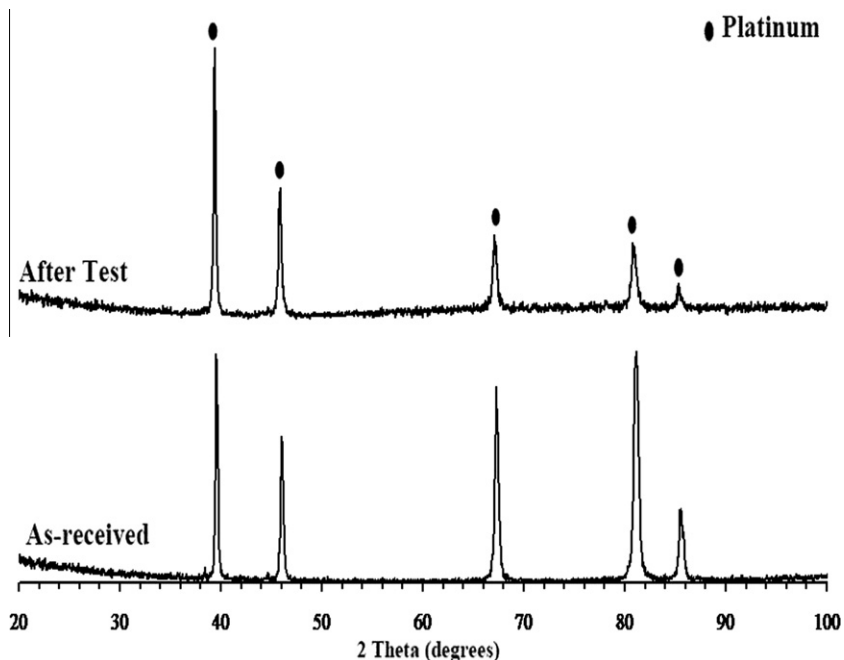


**Fig. 16.** X-ray diffraction (XRD) patterns of the platinum reference electrode before and after the electrochemical tests which show the characteristic peaks of platinum.

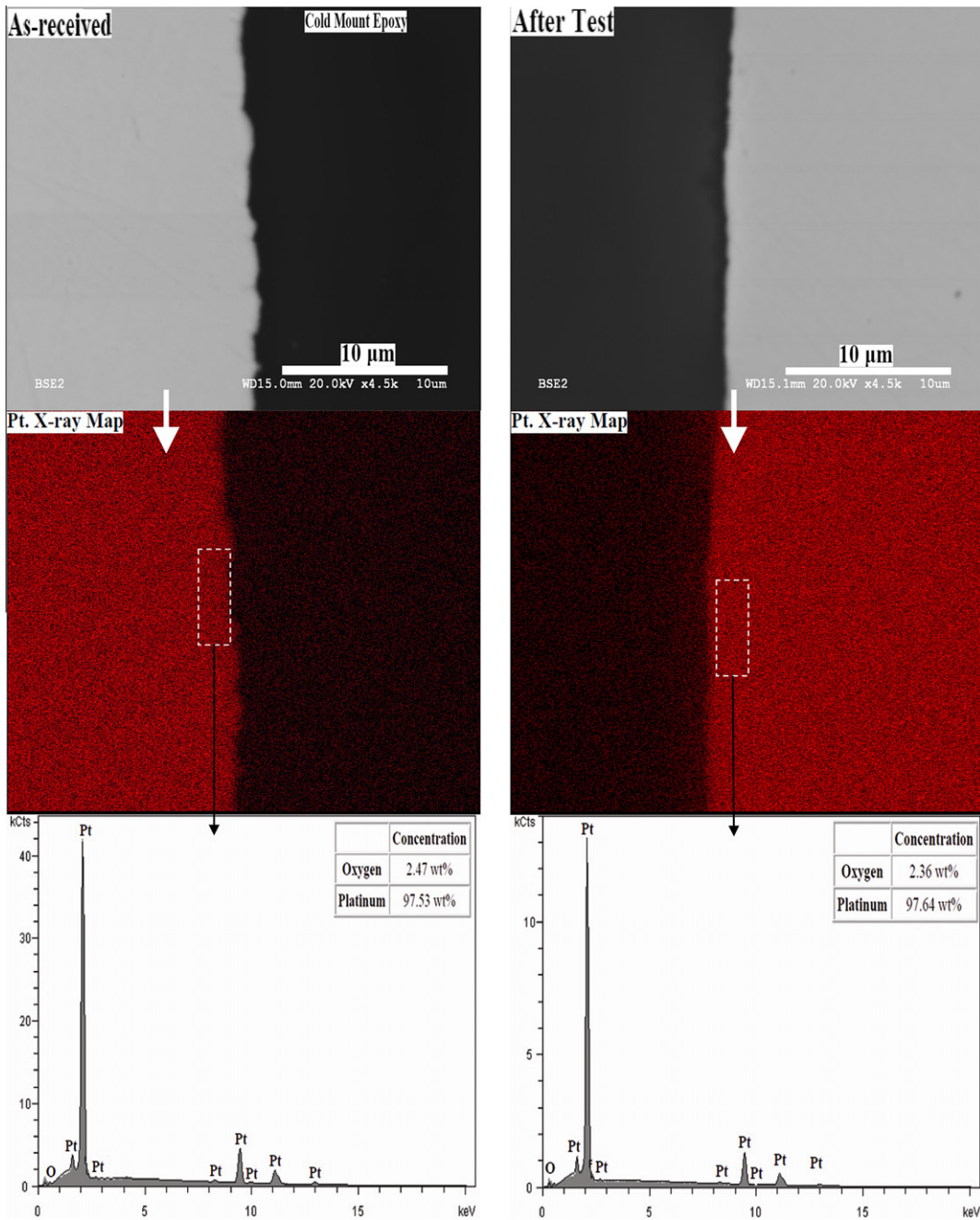


**Fig. 17.** SEM photomicrographs and X-ray mapping of platinum as well as EDX analysis of the platinum wire's cross-section in the as-received condition and after the electrochemical tests in the molten salt medium.

were noted between these two patterns. SEM photomicrographs and EDX analysis from the cross-section of the platinum wire, as well as X-ray mapping of platinum in the as-received condition and after the exposure to the molten salt during the electrochemical tests can be seen in Fig. 17. Obviously, no considerable differences can be observed between these two conditions and no internal oxidation, pitting, surface cracking or surface degradation occurred in the platinum wires samples after the exposure to the molten salt medium. The X-ray mapping of platinum in Fig. 17 confirms that the distribution of platinum in the surface layer of the wire remains completely uniform after the exposure to the molten salt medium and no sign of platinum-depletion/degradation can be observed. Also, results of the weight-loss measurement confirmed

no weight-gain/loss of platinum after the EIS and the potentiodynamic polarization test, when the platinum electrodes were exposed to the molten salt for 24 h at 800, 700 and 600 °C. In summary, platinum exhibited strong resistance to degradation in the molten salt medium and it did not react with the molten phase, which justifies the selection of this metal as a pseudo-reference electrode in the current study.

Furthermore, successful application of platinum (melting point: 1768.3 °C) as a counter and reference electrode for high temperature electrochemical studies has been widely reported in literature, particularly in molten salt environments containing high amounts of heavy metals such as Pb, Zn, and V, as well as high concentrations of Cl and S elements and at temperatures up to 900 °C

[34,47,61,78–84]. This fact confirms that platinum has been known as a reliable pseudo-reference electrode for molten salt-induced corrosion studies.

#### 4. Conclusion

OCP, potentiodynamic polarization, and EIS techniques as well as embedded test and weight-loss measurement method were utilized to study electrochemical properties, corrosion behavior, and degradation mechanisms of alloy 625 beneath 47 PbSO<sub>4</sub>–23 ZnO–13 Pb<sub>3</sub>O<sub>4</sub>–10 Fe<sub>2</sub>O<sub>3</sub>–7 PbCl<sub>2</sub> (wt.%) molten salt mixture under dynamic air atmosphere at 600, 700 and 800 °C. The alloy 625 presented the active dissolution behavior and an anodic film was formed on the surface of the alloy, which was characterized as a non-protective porous corrosion product layer. Underneath the chromium-rich corrosion product layer, a chromium-depleted zone formed. The corrosion product layer mainly consists of chromium, oxygen, and nickel. General surface corrosion, intergranular corrosion, formation of voids and a network of distributed pores on the surface and the cross-section, as well as internal oxidation and sulfidation were identified as different modes of corrosion attack. Based on the XRD data, the characteristic peaks of Ni(Cr<sub>2</sub>O<sub>4</sub>) and Cr<sub>2</sub>O<sub>3</sub> protective layers, provided protectiveness for the alloy against corrosive environments at ambient temperature, completely disappeared/dissolved when the alloy exposed to the molten salt medium at 600, 700 and 800 °C. The dissolution of the protective layers justifies the weak corrosion resistance/appreciable corrosion susceptibility of the alloy 625 in the molten salt environment. High concentration of sulfur and oxygen in the grain boundaries are to blame for the occurrence of the intergranular corrosion together with the internal attack. An electrochemical model (a porous and non-protective barrier layer model) was developed to explain the corrosion/electrochemical behavior of the alloy which fit into the obtained EIS data well.

The highly porous and chromium-rich corrosion product layer acts as the possible diffusion paths for the aggressive species (sulfur and oxygen) of the molten salt to reach the surface of the alloy and diffuse inward mainly through the grain boundaries. This causes the intergranular corrosion process, observed as the internal attacked areas. The grain boundaries were rich in sulfur and oxygen. The transfer of the sulfur from the molten salt to the alloy can be considered as an effective factor on the degradation of the alloy, playing as a propagation mode in the molten salt-induced corrosion of the alloy 625.

#### Acknowledgements

Financial support from Natural Sciences and Engineering Research Council of Canada (NSERC) and Teck Metals Ltd. is gratefully acknowledged. Also, the first author (Ehsan Mohammadi Zahrani) would like to express his gratitude towards the NSERC for providing prestigious Vanier Canada Graduate Scholarship and the University of British Columbia (UBC) for providing the Killam Doctoral Fellowship and Four Years Doctoral Fellowship for him.

#### References

- [1] J.C. Williams, E.A. Starke, Progress in structural materials for aerospace system, *Acta Mater.* 52 (2003) 5775–5799.
- [2] G. Smith, L. Shoemaker, Advanced nickel alloys for coal-fired boiler tubing, *Adv. Mater. Processes* 162 (2004) 23–26.
- [3] D.R. Askeland, *The Science and Engineering of Materials*, second ed., Chapman and Hall, London, 1990.
- [4] R. Chattopadhyay, *Surface Wear: Analysis Treatment and Prevention*, ASM International, Materials Park, OH, 2001.
- [5] G.E. Dieter, *Mechanical Metallurgy*, third Ed., McGraw-Hill, New York, 1986.
- [6] C.T. Sims, N.S. Stoloff, W.C. Hagel, *Superalloys II: High Temperature Materials for Aerospace and Industrial Power*, John Wiley & Sons, New York, 1987.
- [7] H. Sun, X. Wu, E. Han, Effects of temperature on the protective property, structure and composition of the oxide film on alloy 625, *Corros. Sci.* 51 (2009) 2565–2572.
- [8] S.E. Ziemiak, M. Hanson, Corrosion behavior of NiCrMo alloy 625 in high temperature, hydrogenated water, *Corros. Sci.* 45 (2003) 1595–1618.
- [9] N. Espallargas, S. Mischler, Tribocorrosion behaviour of overlay welded Ni–Cr 625 alloy in sulfuric and nitric acids: electrochemical and chemical effects, *Tribol. Int.* 43 (2010) 1209–1217.
- [10] J. Adamiec, High temperature corrosion of power boiler components cladded with nickel alloys, *Mater. Charact.* 60 (2009) 1093–1109.
- [11] H.Y. Al-Fadhl, J. Stokes, M.S.J. Hashmi, B.S. Yilbas, HVOF coating of welded surfaces: fatigue and corrosion behaviour of stainless steel coated with Inconel-625 alloy, *Surf. Coat. Technol.* 200 (2006) 4904–4908.
- [12] Z.W. Zhong, Z.F. Peng, N. Liu, Surface roughness characterization of thermally sprayed and precision machined WC–Co and alloy-625 coatings, *Mater. Charact.* 58 (2007) 997–1005.
- [13] T.S. Sidhu, R.D. Agrawal, S. Prakash, Hot corrosion of some superalloys and role of high-velocity oxy-fuel spray coatings—a review, *Surf. Coat. Technol.* 198 (2005) 441–446.
- [14] L. Nylof, E. Hagglom, Corrosion of experimental superheater alloys in waste fuel combustion, in: *Corrosion/97*, Nace International, Houston, TX, Paper No. 154, 1997.
- [15] E. Mohammadi Zahrani, C. Cuevas-Arteaga, D. Verhelst, A. Alfantazi, High temperature corrosion of 625 superalloy under iron–zinc–lead oxide/sulfate/chloride salt mixtures, *ECS Trans.* 28 (2010) 171–185.
- [16] A. Philip, P.E. Schweitzer, *Fundamentals of Metallic Corrosion: Atmospheric and Media Corrosion of Metals*, CRC Press, New York, 2007.
- [17] F. Wang, Y. Shu, Influence of Cr content on the corrosion of Fe–Cr alloys: the synergistic effect of NaCl and water vapour, *Oxid. Met.* 59 (2003) 201–214.
- [18] H.J. Grabke, M. Spiegel, A. Zhas, The role of alloying elements and carbides in the chloride-induced corrosion of steels and alloys, *Mater. Res.* 7 (2004) 89–95.
- [19] F.J. Martin, P.M. Natishan, K.E. Lucas, E.A. Hogan, A.M. Grolleau, E.D. Thomas, Crevice corrosion of alloy 625 in natural seawater, *Corrosion* 59 (2003) 498–504.
- [20] G.D. Smith, D.J. Tillack, S.J. Patel, in: E.A. Loria (Ed.), *Fifth International Symposium on Superalloys 718, 625, 706 and Various Derivatives*, TMS: The Minerals, Metals & Materials Society, Pittsburgh, PA, 2001, pp. 35.
- [21] C.S. Tedmon, D.A. Vermilyea, Carbide sensitization and intergranular corrosion of nickel base alloys, *Corrosion* 27 (1971) 376–381.
- [22] E. Otero, A. Pardo, J. Hernaez, F.J. Perez, The hot corrosion of in-657 superalloy in Na<sub>2</sub>SO<sub>4</sub>–V<sub>2</sub>O<sub>5</sub> melt eutectic, *Corros. Sci.* 32 (1991) 677–683.
- [23] T.S. Sidhu, S. Prakash, R.D. Agrawal, Hot corrosion and performance of nickel-based coatings, *Curr. Sci.* 90 (2006) 41–47.
- [24] S. Lee, N.J. Themelis, M.J. Castaldi, High-temperature corrosion in waste-to-energy boilers, *J. Therm. Spray Technol.* 16 (2007) 104–110.
- [25] H. Zwather, Ways to Improve the Efficiency of Waste to Energy Plants for the Production of Electricity and Reusable Materials, 11th North America WTE conference, Florida, Tampa, 2003.
- [26] G.H. Meier, A review of advances in high-temperature corrosion, *Mater. Sci. Eng.*, A 120–121 (1989) 1–11.
- [27] A.S. Khanna, S.K. Jha, Degradation of materials under hot corrosion conditions, *Trans. Indian Inst. Met.* 51 (1988) 279–290.
- [28] F.S. Pettit, C.S. Giggins, Hot corrosion, in: C.T. Sims, N.S. Stoloff, W.C. Hagel (Eds.), *Superalloys II*, John Wiley & Sons, New York, NY, 1987.
- [29] Y. Kawahara, High temperature corrosion mechanisms and effect of alloying elements for materials used in waste incineration environment, *Corros. Sci.* 44 (2002) 223–245.
- [30] R.A. Rapp, Y.S. Zhang, Hot corrosion of materials: fundamental studies, *JOM* 46 (1994) 47–55.
- [31] P. Hancock, Vanadic and chloride attack of superalloys, *Mater. Sci. Technol.* 3 (1987) 536–544.
- [32] I.G. Wright, High-temperature corrosion, in: *Metals Handbook*, ninth ed., Materials Park, vol. 13, ASM, 1987, pp. 97–103.
- [33] Y. Kawahara, Evaluation of high-temperature corrosion life using temperature gradient corrosion test with thermal cycle component in waste combustion environment, *Mater. Corros.* 57 (2006) 60–72.
- [34] E. Mohammadi Zahrani, A. Alfantazi, Corrosion behavior of alloy 625 in PbSO<sub>4</sub>–Pb<sub>3</sub>O<sub>4</sub>–PbCl<sub>2</sub>–ZnO–10 wt.% CdO molten salt medium, *Metall. Mater. Trans. A* 43 (2012) 2857–2868.
- [35] C. Cuevas-Arteaga, D. Verhelst, A. Alfantazi, Performance of alloy 625 under combustion gas environments: a review, *ECS Trans.* 28 (2010) 61–67.
- [36] J.R. Davis, *ASM Specialty Hand Book: Nickel, Cobalt and their Alloys*, ASM International, Materials Park, OH, 2000, pp. 301.
- [37] Standard Guide for Preparation of Metallographic Specimens, American Society for Testing and Materials, ASTM E3–11, 2011, pp. 1–13.
- [38] Standard Test Method for Determining Average Grain Size, American Society for Testing and Materials, ASTM E112–10, 2010, pp. 1–26.
- [39] W.M. Lu, T.J. Pan, K. Zhang, Y. Niu, Accelerated corrosion of five commercial steels under ZnCl<sub>2</sub>–KCl deposit in a reducing environment typical of waste gasification at 673–773 K, *Corros. Sci.* 50 (2008) 1900–1906.
- [40] J. Di Martino, C. Rapin, P. Berthod, R. Podor, P. Steinmetz, Corrosion of metals and alloys in molten glasses. Part 1: glass electrochemical properties and pure metal (Fe, Co, Ni, Cr) behaviours, *Corros. Sci.* 46 (2004) 1849–1864.
- [41] B. Zhu, G. Lindbergh, D. Simonsson, Comparison of electrochemical and surface characterization methods for investigation of corrosion of bipolar plate

- materials in molten carbonate fuel cell: part I. Electrochemical study, *Corros. Sci.* 41 (1999) 1497–1513.
- [42] Y. Niu, S. Wang, F. Gao, Z.G. Zhang, F. Gesmundo, The nature of the third-element effect in the oxidation of Fe-xCr-3 at % Al alloys in 1 atm O<sub>2</sub> at 1000 °C, *Corros. Sci.* 50 (2008) 345–356.
- [43] A. Ruh, M. Spiegel, Thermodynamic and kinetic consideration on the corrosion of Fe, Ni and Cr beneath a molten KCl-ZnCl<sub>2</sub> mixture, *Corros. Sci.* 48 (2006) 679–695.
- [44] M. Tanaka, K. Kashiwagi, N. Kawashima, S. Kitaoka, O. Sakurada, Y. Ohya, Effect of grain boundary cracks on the corrosion behaviour of aluminum titanate ceramics in a molten aluminum alloy, *Corros. Sci.* 54 (2012) 90–96.
- [45] Y.I. Sannikov, M.A. Liamina, V.A. Shumskij, M.V. Radashin, A physical and chemical description of the Kivcet lead flash smelting process, *CIM Mag.* 91 (1998) 76–81.
- [46] Pollution Prevention and Abatement Handbook, Lead and Zinc Smelting, The World Bank Group, Washington, DC, 1998, pp. 332–336.
- [47] J.I. Barraza-Fierro, M.A. Espinosa-Medina, M. Hernandez-Hernandez, H.B. Liu, E. Sosa-Hernandez, Effect of Li and Cu addition on corrosion of Fe-40 at.% Al intermetallics in molten LiCl-KCl eutectic salt, *Corros. Sci.* 59 (2012) 119–126.
- [48] C.A.C. Sequeira, Fundamentals of Molten Salt Corrosion, in: C.A.C. Sequeira (Ed.), High Temperature Corrosion in Molten Salts in Molten Salt Forum, Trans Tech Publications Ltd., United Kingdom, 2003, pp. 3–40.
- [49] Standard Test Method for Conducting Potentiodynamic Polarization Resistance Measurements, American Society for Testing and Materials, ASTM G59–97, 2009, pp. 1–4.
- [50] Standard Reference Test Method for Making Potentiostatic and Potentiodynamic Anodic Polarization Measurements, American Society for Testing and Materials, ASTM G5–94, 2004, pp. 1–12.
- [51] Y. Zou, J. Wang, Y.Y. Zheng, Electrochemical techniques for determining corrosion rate of rusted steel in seawater, *Corros. Sci.* 53 (2011) 208–216.
- [52] Standard Practice for Preparing, Cleaning, and Evaluating Corrosion Test Specimens, American Society for Testing and Materials, ASTM G1-03, 2011, pp. 1–9.
- [53] Standard Practice for Laboratory Immersion Corrosion Testing of Metals, American Society for Testing and Materials, ASTM G31–72, 2004, pp. 1–8.
- [54] ISO, Corrosion of Metals and Alloys – Method for Metallographic Examination of Samples after Exposure to High-temperature Corrosive Environments, International Organization for Standardization, ISO/DIS 26146, 2011, pp. 1–11.
- [55] A. Firouzi, K. Shirvani, The structure and high temperature corrosion performance of medium-thickness aluminide coatings on nickel-based superalloy GTD-111, *Corros. Sci.* 52 (2010) 3579–3585.
- [56] M. Durand-Charre, The Microstructure of Superalloys, Gordon & Breach Science Publishers, Amsterdam, 1997.
- [57] R.A. Ricks, A.J. Porter, R.C. Ecob, The growth of gamma prime precipitates in nickel-base superalloys, *Acta Metall.* 31 (1983) 43–53.
- [58] M.S.A. Karunaratne, R.C. Reed, Interdiffusion of the platinum group metals in nickel at elevated temperatures, *Acta Mater.* 51 (2003) 2905–2919.
- [59] R.C. Reed, The superalloys: Fundamentals and Applications, Cambridge University Press, New York, 2006.
- [60] A. Martínez-Villafañe, F. Almeraya-Calderón, C. Gaona-Tiburcio, J. Chacón-Nava, G. González-Rodríguez, Evaluation of corrosion resistance of two engineering alloys in molten salts by electrochemical techniques, *Mater. Corros.* 54 (2003) 32–36.
- [61] M.A. Espinosa-Medina, G. Carbajal-De la Torre, H.B. Liu, A. Martínez-Villafañe, J.G. González-Rodríguez, Hot corrosion behaviour of Fe-Al based intermetallic in molten NaVO<sub>3</sub> salt, *Corros. Sci.* 52 (2009) 1420–1427.
- [62] D.M. Farrell, F.H. Stott, Proceeding of UK corrosion conference, The Institute of Corrosion, Manchester, 1991, pp. 1–14.
- [63] M. Montgomery, O. Biede, O.H. Larson, Experiences with Inconel 625 in biomass and waste incineration plants, *Mater. Sci. Forum* 522–523 (2006) 523–530.
- [64] R.E. Reed-Heel, R. Abbaschian, Physical Metallurgy Principles, third Ed., PWS Publishing Company, Boston, MA, 1994.
- [65] D.J. Young, High Temperature Oxidation and Corrosion of Metals, in: Tim Burstein (series Ed.), first ed., Elsevier Corrosion Series, Elsevier, London, 2008.
- [66] R.C. John, Engineering assessment of oxidation of engineering alloys, NACE Corrosion Conference, NACE International, Houston, TX, 1996, pp. 171.
- [67] F.S. Pettit, G.H. Meier, M. Gell, C.S. Kartovich, R.H. Bricknel, W.B. Kent, J.F. Radovitch, Oxidation and Hot Corrosion of Superalloys In Superalloys, The Metals Society of AIME, Warrendale, PA, 1984, pp. 651.
- [68] S.R.J. Saunders, Corrosion in the presence of melts and solids, in: H.J. Grabke, D.B. Meadowcroft (Eds.), Guidelines for Methods of Testing and Research in High Temperature Corrosion, The Institute of Materials, London, 1995.
- [69] N. Bircks, G.H. Meier, F.S. Pettit, Introduction to the High Temperature Oxidation of Metals, second ed., Cambridge University Press, 2006.
- [70] R.A. Rapp, Hot corrosion of materials: a fluxing mechanism?, *Corros. Sci.* 44 (2002) 209–221.
- [71] K. Hladky, L.M. Callow, J.L. Dawson, Corrosion rates from impedance measurements: an introduction, *Br. Corros. J.* 15 (1980) 20–25.
- [72] R.M. Carranza, M.G. Alvarez, The effect of temperature on the passive film properties and pitting behaviour of a Fe-Cr-Ni alloy, *Corros. Sci.* 38 (2009) 909–925.
- [73] B. Beverskog, M. Bojinov, A. Englund, P. Kinnunen, T. Laitinen, K. Mäkelä, T. Saario, P. Sirkia, A mixed-conduction model for oxide films on Fe, Cr and Fe-Cr alloys in high-temperature aqueous electrolytes-I. Comparison of the electrochemical behaviour at room temperature and at 200 °C, *Corros. Sci.* 44 (2002) 1901–1921.
- [74] F.J. Perez, J. Nieto, J.A. Trilleros, M.P. Hierro, Hot corrosion monitoring of waste incineration corrosion processes using electrochemical techniques, *Mater. Sci. Forum* 522–523 (2006) 531–538.
- [75] F.J. Perez, M.P. Hierro, J. Nieto, Waste incineration corrosion processes: oxidation mechanisms by electrochemical impedance spectroscopy, *Mater. Corros.* 59 (2008) 566–572.
- [76] T. Ishitsuka, K. Nose, Stability of protective oxide films in waste incineration environment-solubility measurement of oxide in molten chloride, *Corros. Sci.* 44 (2002) 247–263.
- [77] B.P. Montany, D.A. Shores, Role of chlorides in hot corrosion of a cast Fe-Cr-Ni alloy. Part I: experimental studies, *Corros. Sci.* 46 (2004) 2893–2907.
- [78] C.L. Zeng, W. Wang, W.T. Wu, Electrochemical impedance models for molten salt corrosion, *Corros. Sci.* 43 (2001) 787–801.
- [79] A. Otero, A. Pardo, F.J. Perez, M.V. Utrilla, T. Levi, Corrosion behaviour of 12CrMoV steel in waste incineration environments: hot corrosion by molten chloride, *Oxid. Met.* 49 (1998) 467–483.
- [80] C. Cuevas-Arteaga, Corrosion study of HK-40m alloy exposed to molten sulfate/vanadate mixtures using the electrochemical noise technique, *Corros. Sci.* 50 (2008) 650–663.
- [81] C. Cuevas-Arteaga, U. Uruchurtu, J. González, G. Izquierdo-Montalvo, J. Porcayo Calderón, U. Cano-Castillo, Corrosion evaluation of alloy 800 in sulfate/vanadate molten salt, *Corrosion* 60 (2004) 548–560.
- [82] C. Cuevas-Arteaga, J. Uruchurtu-Chavarín, J. Porcayo-Calderon, G. Izquierdo Montalvo, J. González, Study of molten salt corrosion of HK-40m alloy applying linear polarization resistance and conventional weight loss techniques, *Corros. Sci.* 46 (2004) 2663–2679.
- [83] M.A. Espinosa, G. Carbajal De la Torre, J. Parcayo-Calderon, A. Martínez-Villafañe, J.G. Chacón-Nava, M. Casales, J.G. Gonzalez-Rodríguez, Corrosion of atomized Fe40Al based intermetallics in molten Na<sub>2</sub>SO<sub>4</sub>, *Mater. Corros.* 54 (2003) 304–310.
- [84] M.A. Espinosa-Medina, M. Casales, A. Martínez-Villafañe, J. Porcayo-Calderon, L. Martínez, J.G. Gonzalez-Rodríguez, Hot corrosion of atomized iron aluminides doped with boron and reinforced with alumina, *Mater. Sci. Eng A* 300 (2001) 183–189.